NASA CONTRACTOR
REPORT

NASA CR-129037

(NASA-CR-129037) PHYSICAL FORCES INFLUENCING SKYLAB EXPERIMENTS M551, M552, AND M553 Summary Report (Lockheed Missiles and Space Co.) 77 p HC $4.75
CSCL 22C G3/12

N75-10117

Unclas
51124

PHYSICAL FORCES INFLUENCING SKYLAB EXPERIMENTS M551, M552, and M553

Summary Report

By S. V. Bourgeois
Lockheed Missiles and Space Company, Inc.
Huntsville, Alabama

January 1974

Prepared for

NASA-GEORGE C. MARSHALL SPACE FLIGHT CENTER
Marshall Space Flight Center, Alabama 35812

TECHNICAL REPORT STANDARD TITLE PAGE

1. REPORT NO.	2. GOVERNMENT ACCESSION NO.	3. RECIPIENT'S CATALOG NO.
NASA CR-129037		

4. TITLE AND SUBTITLE	5. REPORT DATE
Physical Forces Influencing Skylab Experiments M551, M552 and M553	January 1974
	6. PERFORMING ORGANIZATION CODE
7. AUTHOR(S)	8. PERFORMING ORGANIZATION REPORT #
S. V. Bourgeois	TR D390056
9. PERFORMING ORGANIZATION NAME AND ADDRESS	10. WORK UNIT NO.
Lockheed Missiles and Space Company, Inc. Huntsville, Alabama	11. CONTRACT OR GRANT NO. NAS 8-27015
12. SPONSORING AGENCY NAME AND ADDRESS	13. TYPE OF REPORT & PERIOD COVERED
National Aeronautics and Space Administration Washington, D.C., 20546	Contractor Report
	14. SPONSORING AGENCY CODE

15. SUPPLEMENTARY NOTES

16. ABSTRACT

This report summarizes the physical forces influencing Skylab experiments M551, M552 and M553 and was compiled under Contract NAS8-27015. This effort was performed by the Lockheed-Huntsville Research and Engineering Center for NASA-Marshall Space Flight Center.

The NASA Contracting Officer's Representative (COR) for this study is Mr. T. C. Bannister, S&E-SSL-T. The NASA principal investigators for this study are Mr. R. M. Poorman (M551), S&E-ASTN-MM; Mr. J. R. Williams (M552), S&E-PT-M; and Mr. E. A. Hasemeyer (M553), S&E-PT-MWM.

The author also acknowledges the other investigators whose results contributed to this report: C. M. Adams, University of Wisconsin; M. R. Brashears, Lockheed Missile & Space Company; D. N. Braski, Union Carbide Corporation; J. L. Brown, Georgia Institute of Technology; P. C. Johnson, A. D. Little Company; T. Z. Kattamis, University of Connecticut; D. J. Larson, Grumman Aerospace Corporation; K. Masubuchi, Massachusetts Institute of Technology; R. E. Monroe, Battelle Memorial Institute; J. M. Tobin, Westinghouse Electric Corporation; and W. A. Zisman, Naval Research Laboratory.

17. KEY WORDS	18. DISTRIBUTION STATEMENT
	Unclassified - Unlimited

W K Vaudamme

19. SECURITY CLASSIF. (of this report)	20. SECURITY CLASSIF. (of this page)	21. NO. OF PAGES	22. PRICE
Unclassified	Unclassified	76	NTIS

FOREWORD

This report summarizes the physical forces influencing Skylab experiments M551, M552 and M553 and was compiled under Contract NAS8-27015. This effort was performed by the Lockheed-Huntsville Research & Engineering Center for NASA-Marshall Space Flight Center.

The NASA Contracting Officer's Representative (COR) for this study is Mr. T. C. Bannister, S&E-SSL-T. The NASA principal investigators for this study are Mr. R. M. Poorman (M551), S&E-ASTN-MM; Mr. J. R. Williams (M552), S&E-PT-M; and Mr. E. A. Hasemeyer (M553), S&E-PT-MWM.

The author also acknowledges the other investigators whose results contributed to this report: C. M. Adams, University of Wisconsin; M. R. Brashears, Lockheed Missiles & Space Company; D. N. Braski, Union Carbide Corporation; J. L. Brown, Georgia Institute of Technology; P. C. Johnson, A. D. Little Company; T. Z. Kattamis, University of Connecticut; D. J. Larson, Grumman Aerospace Corporation; K. Masubuchi, Massachusetts Institute of Technology; R. E. Monroe, Battelle Memorial Institute; J. M. Tobin, Westinghouse Electric Corporation; and W. A. Zisman, Naval Research Laboratory.

TABLE OF CONTENTS

TABLE OF CONTENTS (Continued)

LIST OF ILLUSTRATIONS

LIST OF TABLES

NOMENCLATURE

A	Area
B	Magnetic Induction
C	Heat Capacity
c	Concentration, Mass or Moles per Unit Volume
D	Diameter, Diffusivity, Displacement Current
d	Differential Operator
E	Electric Field Intensity
e	Base of Natural Logarithms
F	Force
f	Force Component
G	Temperature Gradient of the Melt at Solidification Front
g	Acceleration of Gravity
g_E	Sea Level Gravity on Earth, 9.8 m/sec^2
H	Magnetic Field Intensity
h	Individual Coefficient of Heat Transfer
I	Electrical Current Intensity
K	Coefficient of Isothermal Volumetric Compressibility, $\frac{1}{\rho}\left(\frac{\partial \rho}{\partial P}\right)_T$
k	Mass Transfer Coefficient, Thermal Conductivity
L	Length
M_w	Molecular Weight
m	Slope of Equilibrium Curve

NOMENCLATURE (Continued)

$\dot{m}$	Mass Flux Due to Evaporation
N_i	Mole Fraction of Component i
$\vec{n}$	Unit Normal Vector
n_i	Moles of Component i
P	Pressure, Power, Temperature Rate (^{o}K/sec)
P_V	Vapor Pressure
p	Partial Pressure
$\dot{Q}$	Rate of Internal Heat Generation
q	Heat
$\dot{q}$	Rate of Heat Flow
R	Universal Gas Constant, Resistance, Outer Radius, Crystal Interface Growth Rate
r	Radius
S	Surface Tension Gradient with Temperature
T	Temperature
T_M	Melting Point
ΔT	Degree of Undercooling
t	Time
U	Internal Energy
u	Longitudinal Component of Local Velocity, Velocity in General
V	Volume
$\vec{V}$	Velocity Vector
v	Lateral Component of Local Velocity, Nominal Velocity

w	Normal Component of Local Velocity
x	Longitudinal Distance from Datum Plane
y	Lateral Distance from Datum Plane
z	Vertical Distance from Datum Plane

GREEK LETTERS

α	Thermal Diffusivity
β	Coefficient of Isobaric Volumetric Thermal Expansion, $\frac{1}{\rho}\left(\frac{\partial \rho}{\partial T}\right)_P$
γ	Ratio of Specific Heats, Ratio of Buoyancy over Surface Tension Force
∇	Grad or del Operator
∂	Partial Differential Operator
δ	Position of Melt/Crystal Interface, Boundary Layer Width, Variation Operator
Δ	Difference, Finite Difference Operator
ϵ	Emissivity (Radiation)
ϵ'	Permittivity (Dielectric Constant)
η	Efficiency
θ	Contact Angle
λ	Latent Heat of Phase Change, Wave Length, Interlammellar Eutectic Spacing
λ_f	Latent Heat of Fusion
λ_s	Latent Heat of Sublimation

NOMENCLATURE (Continued)

λ_v	Latent Heat of Vaporization
μ	Viscosity
μ'	Magnetic Permeability
ν	Kinematic Viscosity
ρ	Density, Electrical Resistivity
ρ_e	Electrical Charge Density
σ	Surface Tension, Stefan-Boltzmann Constant
σ_{LV}	Surface Energy at Liquid-Vapor Interface
σ_{LS}	Surface Energy at Liquid-Solid Interface
σ_{SV}	Surface Energy at Solid-Vapor Interface
σ'	Electrical Conductivity
ϕ	Angle
Φ	Viscous Dissipation
ω	Frequency, Angular Velocity

DIMENSIONLESS NUMBERS

Bo	Bond Number, $\rho g L^2/\sigma$ or $\rho g L^2/ST$
N_{MI}	Magnetic Interaction Number, $B^2/L/2\mu' ST$
Ma	Marangoni Number, $S\Delta T L/\rho\nu\alpha$
Ma_c	Critical Marangoni Number
Nu	Nusselt Number, hL/k
Oh	Ohnesorge Number, $\mu/\sqrt{\rho LST}$
Pr	Prandtl Number, $\mu C/k$

Ra	Rayleigh Number, $g\beta\Delta TL^3/\nu\alpha$
Ra_c	Critical Rayleigh Number
St	Stokes Number, $\mu t/\rho L$
Sf	Stefan Number, $\sigma T^3 L/k$
We	Weber Number, $\rho v^2 L/\sigma$

SUBSCRIPTS

c	Critical
f	Fraction
G	Vapor
i	Generalized Component, Interface
j	Generalized Component
L	Liquid, Liquidus
M	Melting Point
m	Mean
o	Initial
P	Constant Pressure
S	Solidus, Solid
s	Surface
T	Constant Temperature, Total
t	Tangential, Terminal
V	Constant Volume, Vapor Phase
W	Wall

SUPERSCRIPTS

$\rightarrow$	Denotes Vector Quantity
$\cdot$	First Derivative with Time
$\cdot\cdot$	Second Derivative with Time

SECTION I. INTRODUCTION

This summary report on physical forces is concerned specifically with the Metals Melting Experiment, the Exothermic Brazing Experiment, and the Sphere Forming Experiment. They were performed in the M512 facility during the Skylab I mission of May-June 1973 by Astronaut Charles Conrad. These experiments are described briefly as follows:

M551 Metals Melting Experiment: Three sample disks, each containing three metal specimens of varying thicknesses, are to be rotated automatically at a controlled speed of 2.5 rpm under an electron beam gun such that an electron beam weld seam is produced in the metal specimen at a radius of 6 cm. Disk materials include 2219 aluminum, 321 stainless steel and tantalum. During the continuous weld portion of each disk, both full and partial penetration of the disk will be achieved by having a constant power input but a varying disk thickness. For each disk, the continuous weld will be followed by a dwell portion. In the dwell portion of the weld, the disk will remain stationary while the electron beam impinges on a thick segment of the disk, thus creating a large molten pool. The electron beam will then be shut off and the pool will be allowed to solidify.

M552 Exothermic Brazing: A technique for joining stainless steel tubes will be tested in this experiment and the flow and solidification behavior of weightless molten braze alloys will be studied. The joining technique will use a solid mixture that produces heat by exothermic chemical reaction to braze sleeves over 18.75-mm diameter tubes, using a copper-silver-lithium braze alloy. A package containing four assemblies, each consisting of a tube with sleeve and preformed braze alloy surrounded by exothermic material, will be mounted in the M512 facility's vacuum chamber. The exothermic reactions in the four assemblies will be ignited in sequence and the whole package will be returned to earth for analysis.

M553 Sphere Forming Experiment: Twenty-eight 6.35-mm diameter spherical specimens will be cast using the electron beam gun as a heat source. The specimens will be initially supported on two wheels by a sting. After melting is completed, the spheres will then be separated from their stings and allowed to solidify while free-floating in the vacuum chamber. Specimens will consist of the following materials: pure nickel, Ni-1% Ag, Ni-30% Cu, and Ni-12% Sn.

The M512 facility consisted of a spherical processing chamber, approximately 40 cm in diameter in which several experiments were performed. The electron beam in the M512 unit was operated between 50 to 80 mA at 20 kV. A vacuum environment of 10^{-4} torr was created by venting the chamber directly to outer space.

The nature, magnitude and direction of the physical forces which influence the experiments are important because they control the liquid dynamics of the molten metals. Fluid motions, in turn, affect the melting and solidification of the metals. Thus, the quality of the processed specimens depends on the physical forces and their attendant effects on liquid motions.

For these particular Skylab experiments, the only significant difference between space and earth processing will be the lack of gravity. The maximum gravity level experienced during operation of the M551, M552 and M553 experiments aboard Skylab II was 7×10^{-4} g_E ($g_E = 9.8$ m/sec^2). Other environmental factors which may also differ from earth processing are the vacuum, radiation, electromagnetic and thermal conditions.

Gravity has no direct effect on grain structure or other properties of solidified material. These properties are determined by the crystallization kinetics which are controlled by short-range intermolecular forces; i.e., the temperature and concentration at the fluid-solid interface. Gravity has not been shown to have any significant direct effect on these forces, but can affect solidification indirectly through its direct effect on fluid motion. The three major indirect effects of gravity on solidification are:

- Sedimentation
- Buoyancy-Induced Convection, and
- Hydrostatic Pressure.

In addition to these three very important indirect effects, the lack of gravity will also afford the study of a more direct effect — the opportunity to obtain homogeneous nucleation. The long free-float times potentially available in space processing applications will allow melts to cool and nucleate without the deleterious effects of container walls. Wall effects are usually very strong in nucleation phenomena and prevent large degrees of supercooling from being attained in terrestrial processing. These effects are explained further below.

Sedimentation: This effect may be significant whenever heterogeneous mixtures exist in fluids, such as in monotectic, dispersed-particle, or fiber-reinforced composite casting. The denser of the

immiscible materials will tend to settle unless colloidal or electrostatic attractions interfere. Also, in supercooled melts, segregation of freshly formed nuclei by gravity would affect the final grain structure. Nonmetallic inclusions, gas bubbles and voids, which usually exist in melts, are also distributed nonuniformly by gravity.

Convection: In terrestrial processing, gravity is the primary driving force for the convection of contained fluids when they are subjected to thermal or concentration gradients. Temperature gradients arise from external heating and cooling, whereas concentration gradients are usually produced internally (Soret effect and solute rejection at interfaces which leads to "constitutional super-cooling"). These two gradients can produce density gradients large enough to induce buoyancy-driven flow. This fluid motion affects the temperature and concentration profiles within the fluid. This subsequently alters the shape and rate of movement of the freezing interface, because the kinetics of freezing depend on the local temperature and concentration. The degree of mixing caused by convection may be large enough to change the rate of solidification from kinetic to heat transfer or diffusion controlled which could drastically alter the grain structure. Examples of this convective effect on the transitions from planar to cellular or dendritic growth, from columnar to equiaxed eutectic structures, and from unidirectional to colonied or banded eutectic structures are cited frequently in the literature. Another effect of gravity-driven convection on solidification processes is that the bulk fluid movement, if rapid enough, can break delicate dendrite arms and therby alter final grain structure. Furthermore, interlamellar spacing in eutectic growth and dendrite arm spacing are dependent on cooling rate which is a strong function of convection.

Hydrostatic Pressure: A body of fluid in a gravity field sustains a vertical pressure gradient as the bottom fluid must support the weight of the upper fluid. This pressure gradient distorts the shape of liquids on earth because the shape of a liquid surface is determined by the surface tension and the internal hydrostatic pressure (and adhesion if the liquid wets a solid surface). Distorted drops of liquid will result in nonsymmetrical solids upon freezing.

Homogeneous Nucleation Effects: Microgravity solidification in the M553 experiment may lead to containerless freezing which offers the probability of homogeneous nucleation and attendant large degrees of undercooling. Most of the effects of large undercooling, and thus extremely rapid freezing rates, are beneficial. Increasing the amount of undercooling in an alloy leads to substantial reductions in both the segregation ratio of alloying elements and of dendrite-arm spacings. As a consequence, the rate of homogenization of an alloy increases with increasing undercooling. Other beneficial effects of

undercooling are reduction in grain size, refinement of endogenous inclusions such as silicates and sulfides, and homogeneous distribution of porosity. All these factors are beneficial to mechanical and possibly physical properties of an alloy, such as strength, hardness, electrical resistivity, etc.

The following sections contain separate discussions for each experiment on the physical forces and, where applicable, their effects on molten metal flow and solidification.

SECTION II. M551 METALS MELTING EXPERIMENT

This section contains analyses of the physical forces for the M551 experiment. The first section contains an analysis of the driving forces, magnitude and pattern of natural convective fluid flows which occur in the Metals Melting Experiment. This section is followed by a discourse on the possibility of molten pool spattering due to the momentum of the impinging electron beam. Next the spiking in the partial penetration zone of the stainless steel samples is evaluated for gravity effects. This is followed by a discussion on beading phenomena. Finally expected dwell shape variations and measurements of surface forces for stainless steel are given.

A. CONVECTION ANALYSIS

As in the other M512 experiments, the physical forces and attendant fluid dynamics of the M551 experiment are the most important factors in determining quality of the final product (in this case, the solidified pool, seam and cut produced on various areas of thin metal disks). Flow patterns in the molten material are important in these experiments, because all of the materials have low entropies of fusion [1]. Thus, their solidification (microstructure) is controlled by the rate of heat transfer removal [2], which changes with the flow field [3 and 4]. The flow will be especially important in the dwell mode, since a relatively large pool of melt will be created. The degree of flow will also determine the amount of mixing attained. If no or little flow were present, all heavier components would segregate to the bottom of weld zones on earth, but to a much lesser extent in microgravity environments. Fluid flow can also affect the shape of the weld pool [7].

Application of dimensional analysis [5 and 6] to the governing equations for eb welding, coupled with ground-based and KC-135 experiments, should enable prediction of the extent of reduction or increase of motion in the weld pool and/or the change in flow pattern in electron beam welding in space. Possible physical forces which could induce fluid flow in the M551 experiment, and their causes, include:

- Effective Gravity Force: Resultant force on weld specimen due to earth's gravity and centrifugal and coriolis forces of orbiting spacecraft.
- Lorentz Force: Electromagnetic forces induced by passage of the electron beam current through the specimen.

- Electrostriction: Stresses induced when electrical permittivity changes with density.
- Magnetostriction: Stresses induced when permeability changes with density.
- Electrostatic Force: Caused by presence of excess electrical charge (due to beam current and/or thermionic emission).
- Surface Tension: Tangential stresses at vapor-liquid or liquid-liquid interfaces can be induced if surface tension depends on temperature and/or concentration. Surface tension will also cause pressure gradients across curved interfaces.
- Density Differences Accompanying Phase Changes
- Beam Force: Impinging electrons give up their momentum.
- Thermal Expansion: Dilation and compression of fluids whose density changes appreciably with temperature can induce fluid flow.
- Vibration: Uncontrolled movement due to engine operation, astronaut motion, particle impacts, etc.
- Centrifugal and Coriolis: Generated by disk rotation.
- Vapor Pressure: Evaporating molecules impart momentum which leads to normal stresses at vapor-liquid interface.
- Inertia Forces: Tend to sustain induced motions.
- Viscous Forces: Tend to resist driving forces.

The preceding forces, which could influence fluid flow and solidification, appear explicitly in the conservation equations which apply to formation of a molten pool by electron beam heating. These equations are given in detail in Section IV.

A formal method of determining the controlling physical forces affecting fluid flow and solidification in electron beam welding was introduced in Section IV. The controlling physical forces are determined by nondimensioning the governing differential equations and performing an order-of-magnitude comparison on the various dimensionless groups which result. The key to successful analysis is in choosing the proper reference values; i.e., since no freestream velocity exists, which forces do we equate to estimate a "characteristic" or "typical" velocity. Choosing the proper characteristic velocity is very important, since the reference time, temperature, etc., usually

depend on this velocity. The results arrived at in Section IV are also considered valid for the M551 experiment.

The equation, in dimensionless form, governing electron beam melting is Equation IV.1 shown in Section IV. Values of the pertinent dimensionless groups for each of the M551 materials are given in Table 1. Examining Table 1 in conjunction with Equation IV.1,

Table 1

M551 DIMENSIONAL ANALYSIS

Material	N_{Oh}	N_{Bo}	$\frac{1}{N_{Oh}}$	$\frac{N_{Bo}}{N_{Oh}}$ *	$\frac{N_{Bo}}{N_{Oh}}$ +
2219 Aluminum	5.8×10^{-4}	3.09	1713	5287	0.53
321 Stainless Steel	6.3×10^{-4}	1.56	1581	2461	0.25
Tantalum	3.4×10^{-4}	7.19	2942	21150	2.11

*With Earth gravity ($9.8\ m/sec^2$); +With 10^{-4} Earth gravity.

an order-of-magnitude analysis indicates that surface tension driven convection will occur both in ground tests and for Skylab conditions because $N_{Oh} << 1$. Furthermore, gravity driven convection will exist on ground tests, but will be negligible in the reduced gravity of Skylab. Thus different forces will control convection on earth versus Skylab. The preceding analysis also indicates that electromagnetic or Lorentz forces will be negligible with regard to causing fluid motion. See Section IV for further details.

A review of the literature on electric arc welding, which is somewhat similar to electron beam welding, has generated the following facts which can be compared to the preceding conclusions. In a study of motion in weld pools in arc welding, Woods and Milner [7] conclude that Lorentz forces are the primary cause of motion. An additional secondary cause is the momentum imparted by the impinging arc. Surface tension forces were not considered. Kotecki et al. [8] showed that surface tension and momentum forces of the impinging arc controlled ripple formation in gas tungsten arc welds. Surface tension controls when the arc is shut off. Brimacombe and Weinberg [9] also conclude that surface tension is the driving force for fluid motion once the impinging jet is removed

One direct result of formulating the governing equations is that surface deflection (cutting action) is primarily caused by vapor pressure, but that the beam force is also appreciable. This was determined from the vapor-liquid force equation of Section IV, which indicates that,

$$\frac{\text{Vapor Pressure}}{\text{Beam Pressure}} \approx 2$$

This agrees with earlier studies

Examination of the 24 frames per second flight and ground movies for all three materials indicated agreement with the analytical predictions presented earlier:

- Significant molten metal motion was exhibited in both the dwell and continuous weld molds for both ground and flight tests.
- Surface tension provided an equal magnitude of convection in the dwell pools in microgravity, but the filming speed was too slow to delineate flow patterns.

B. WELD POOL SPLATTERING

In both the M551 and M553 experiments, the heat released to the metal specimens by the impinging electron beam enables a molten pool to form. A question arises as to the stability of these molten liquids in low gravity. At least one of the KC-135 M553 specimens was seen to break up violently into many smaller liquid spheroids upon complete melting. The electron beam was still hitting the specimen during break up. A similar instability might develop in the molten puddle formed during the dwell mode of the M551 experiment, wherein the liquid might not adhere and separate from the solid disk (violent splattering).

There are at least three different mechanisms which might explain the instability observed in the M553 KC-135 specimens. Upon melting, the specimen may have experienced violent degassing which could have led to droplet breakup. Another mechanism might be electrohydrodynamic instability caused by interactions between the electromagnetic forces of the electron beam and the fluid flow field set up in the molten metal by both thermal gradients, Lorentz and other forces [10]. Lastly, the momentum force associated with the impinging electron beam might have set up unstable surface oscillations on the molten metal.

The latter instability mechanism has been treated recently by Berghmans [11]. He performed a theoretical study of fluid interface stability with special attention being given to the role of surface tension. It was motivated by its possible application to the splattering of molten metal as observed during electric arc welding.

Berghmans' study concluded that the weld pool interface would be stable if the following condition was met,

$$We^2 \leq 1.04 + 3.3\ Bo^2 \qquad (II.1)$$

where

We = Weber number

Bo = Bond number

The analysis is only rigorous if inertia and viscous effects are small compared to surface tension effects. Inertia effects are not negligible in the M551 and M553 experiments, but the results of Berghmans' study should give a reasonable approximation.

The criterion expressed by Equation (II.1) was applied to each of the materials in both the M551 (2219 aluminum, stainless steel, and tantalum) and the M553 (pure nickel, Ni-Cu, Ni-Ag, and Ni-Sn) and for gravity levels between ground tests (g_E = 980 cm/sec^2) and those of Skylab ($g = 10^{-5}\ g_E$). Beam diameter was also varied between 0.635 and 0.07 cm. For each of the above cases,

$$We^2 < 10^{-2}$$

therefore, the momentum force of the electron beam will not be a primary cause of weld pool instability in either M551 or M553.

Examination of the 24 frames per second flight and ground movies for all three materials indicated agreement with the analytical predictions presented above. No unstable splattering was evident even in the microgravity environment of Skylab.

C. GRAVITY EFFECTS ON SPIKING

The electron beam welding phenomenon known as spiking occurs in the partial penetration welds of the stainless steel samples in the M551 experiment. This phenomenon is illustrated in Figure 1 which indicates that spiking is caused by oscillation of the melt. Using a pinhole X-ray camera [12] and radiographs of beam-on-plate welds [13] to reveal beam-metal interactions in the cavity

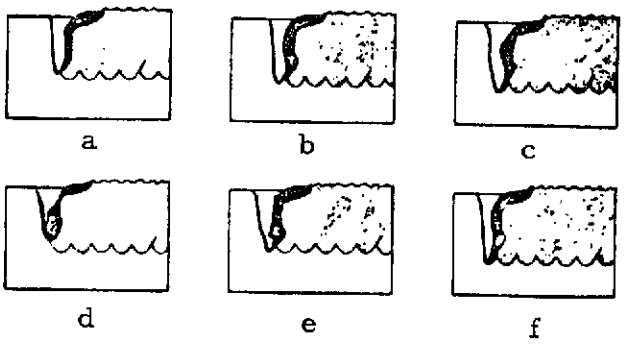

FIGURE 1. SPIKING MECHANISM IN ELECTRON BEAM WELDING

of an electron beam weld, the following mechanism can be proposed for spiking:

> "With initiation of the beam, the beam vaporizes the material as it bores its way into the material. Full penetration is reached within 50 millisec with the establishment of an equilibrium cavity. The beam, impinging on the cavity base, boils heated liquid up the walls of the cavity, most likely in a whirling fashion. Complete metal mixing results due to this dynamic pumping action. Cavity closures are produced as the metal loses kinetic energy. Once a closure forms, it intersects the electron beam producing two effects. First, while the beam is heating the closure, regions below the closure are given time to cool. Second, the closure is heated and generally falls back into the cavity and the cycle recurs. However, the closure may occasionally be vaporized in an explosion. After closure explosion, the cavity is clear of liquid and the beam is again free to impinge on the cavity base causing a spike. However, much more frequently the closure falls back into the cavity. This cyclic mechanism continues (at a typical rate of 150 cycles per sec) as an equilibrium process.
>
> "Spiking results when there is a failure or interruption of the cyclical closure-fallback mechanism. When a closure fails to materialize or is exploded out, the electron beam is free to dwell on the cavity base for a longer time thus producing a penetration spike." [12]
>
> "A spike is formed each time the electron beam penetrates to the base of the weld and the severity of the spiking

depends on the frequency of the oscillation and the welding speed as well as the material being welded.

"When the molten metal flows into the cavity, it can easily trap bubbles of contaminant gases at the base of the weld and, if the cooling rate is sufficiently rapid, the fluid may freeze before the gases can be convected to the surface, thus giving rise to porosity in the fusion zone. Similarly, if the cooling rate is sufficiently rapid, then the melt, as it falls into the cavity, may interrupt the beam long enough for the walls of the spike to freeze so that the fluid, upon falling into the spike, might not bond, thus forming a cold shut or crack.

"The alternate penetration and closing of the cavity are also very efficient in mixing the melt and results in a very homogeneous fusion zone." [13]

A theoretical analysis of the melt-beam dynamics described above and in Figure 1 shows that spiking frequency is predicted by Reference [13].

$$\omega = \frac{\frac{1}{4}\sqrt{\frac{g}{h}}}{\left[\sqrt{\frac{P_V - \frac{2\sigma}{a}}{\rho g h}} - \sqrt{\frac{P_V - \frac{2\sigma}{a} - \rho g h}{\rho g h}}\right]} \qquad \text{(II.2)}$$

where

h = maximum depth of penetration

$2a$ = weld width

g = gravity level

P_V = vapor pressure of molten metal

σ = surface tension of molten metal

ω = spiking frequency

The preceding analysis considered welding a horizontal plate from above. The configuration utilized for M551 ground tests (beam impinges vertical plate from the side at a nine o'clock position with clockwise rotation of the plate past the immobile beam) also lends itself to cavity oscillations as the trailing melt tends to be above the

beam. It should also be pointed out that the above oscillation frequency represents the natural frequency of the cavity. A lower frequency, superimposed over the natural frequency, may occur due to an interaction of the static cavity closing forces (hydrostatic head and surface tension) and the dynamic forces. The dynamic forces arise from the motion of the wave or ripple which is formed in the melt as the cavity penetrates.

Thus Equation (II.2) should not be expected to generate exact, rigorous results to match actual M551 experimental data. It can, however, be utilized to predict a low gravity variation in the stainless steel electron beam welds. As predicted in Equation (II.2), spiking frequency varies inversely with gravity level. Using the experimental conditions, physical properties and beam parameters for the M551 stainless steel experiment and assuming 1120°C of superheat in the melt, Equation (II.2) predicts oscillation frequencies of 22 Hz and 28 Hz for gravity levels of 9.8 m/sec^2 and 9.8×10^{-4} m/sec^2, respectively. At a disk rotation rate of 1.58×10^{-2} m/sec at the beam impingement point, the spikes would be located 0.72 mm apart and 0.56 mm apart in gravity levels of 9.8 m/sec^2 and $9.8\ 10^{-4}$ m/sec^2, respectively. This gravity effect is rapidly dissipated at higher superheats, however, as at 1270°C the spiking frequencies are 41 Hz and 44 Hz at 9.8 m/sec^2 and $9.8\ 10^{-4}$ m/sec^2, respectively. This expected gravity-related variation in spiking will be very difficult to observe because it is very difficult to section radial welds precisely along their centerline and even more difficult to etch, polish and perform metallographic analyses on curved sections. No evidence of this possible variation has been reported to date in any investigations being conducted by other contractors or NASA.

D. BEADING CONSIDERATIONS

Upon examination of the M551 disks, it has been noted that a beading occurs behind the electron beam as the beam moves through the molten material. At present, no detailed analysis has been conducted to explain this phenomenon; however, some consideration has been given to understanding the mechanism. In order to present a hypothesis explaining the proposed mechanism some background information is presented.

The movement of the electron beam cavity through the molten metal resembles the motion of an infinite cylinder (especially if full penetration occurs) through a fluid. It has long been known that such a body leaves in its wake a regular pattern of vortices which move alternately clockwise and counterclockwise and is known as a Karman vortex street. A schematic is presented in Figure 2.

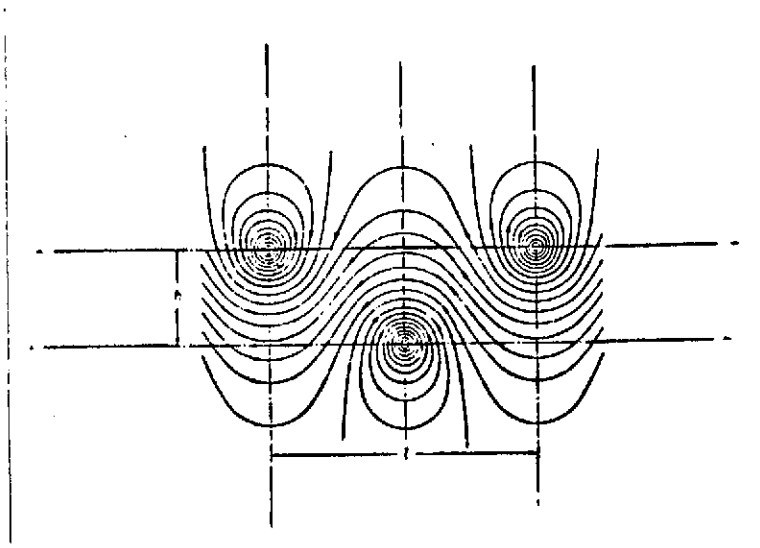

FIGURE 2. KARMAN VORTEX STREET (DIAGRAMMATIC); STREAMLINES DRAWN IN A SYSTEM OF CO-ORDINATES MOVING WITH THE VORTEX STREET

There exists a distinct frequency at which the vortices on one side of the wake are shed that depends only on the Reynolds number of the fluid motion and is given by the Strouhal number, i.e.,

$$S = \frac{fD}{v}$$

where f is the frequency, D is the diameter of the cavity and v is the velocity of the beam in the liquid metal.

From experiment, the relationship of the Strouhal number to the Reynolds number has been determined and is shown in Figure 3. This shows that a critical Reynolds number exists below which no shedding has been observed.

Using these concepts the theoretical number of beads per unit length has been determined for the M551 materials. It should be mentioned that no attempt has been made to account for the solid material (edges) in the cut or the extent of melt in the radial direction of the disks (which is a function of the thermal conductivity). These results are shown in Table 2. The surface tension is included as the magnitude indicates the tendency of the vortices to bead before solidification occurs.

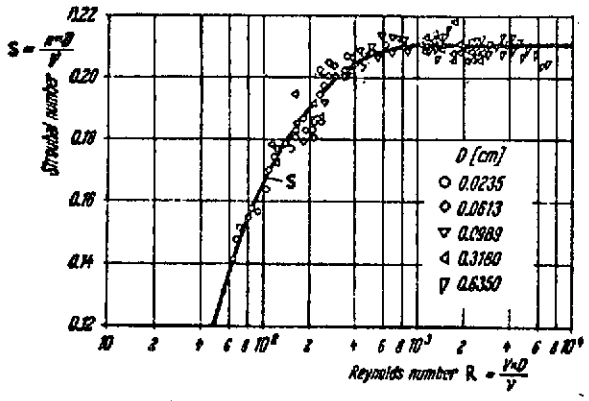

FIGURE 3. STROUHAL NUMBER VS REYNOLDS NUMBER

TABLE 2

BEAD POPULATION

M551 Materials	Reynolds No.	Strouhal No.	Shedding Freq. (beads/ sec)	Beads per cm (on each side)	Total Beads (both sides)	Surface Tension (dynes/ cm)
321 Stainless Steel	55	0.125	0.8	0.5	1.0	1750
2219 Aluminum	86	0.155	1.0	0.6	1.2	737
Tantalum	207	0.19	1.2	0.75	1.5	2150

Some qualitative observations can be made concerning these results. First both aluminum and stainless possess Reynolds numbers near the critical values; thus it would not be surprising if some of the effects not accounted for could have a significant effect on the population of the beads if not controlling whether or not beading will occur. Tantalum, however, possesses the largest Reynolds number and value of surface tension; thus it is expected that these properties produce the greatest probability of beading and will give rise to the greatest population of beads.

Average bead spacing distances were estimated for both flight test and ground based test specimens by inspection of photographs. These experimental values are compared to the predicted values (Table 2) in Table 3.

TABLE 3

BEAD SPACING

M551 Materials	Bead Spacing, cm		
	Theoretical	Flight Test	Ground Based Test
321 Stainless Steel	1.0	1.1	1.1
2219 Aluminum	0.8	—	—
Tantalum	0.7	3.6	2.2

The experimental bead spacing on the stainless steel specimens is seen to be in remarkably good agreement with the predicted value for both flight and ground based tests. No beading is exhibited on the aluminum specimen, however, and the spacing on the tantalum specimen is considerably larger than the predicted value. Consideration was given to the possibility that the departure from vortex shedding theory might be due to "wall" effects resulting from the limitation on the lateral extent of melting. The presence of confining parallel walls will tend to increase the drag force on the cylinder due to the increased fluid velocity in the space between cylinder and wall. This may be considered equivalent to an increased "effective" Reynolds number for drag on the cylinder. Hypothesizing that the Strouhal number relates to this effective Reynolds number according to the relationship in Figure 3, the vortex shedding frequency should be increased by the presence of the confining walls. The results in Table 3, however, indicate the opposite trend. Wall effects, therefore, do not account for the observed departure from vortex shedding theory. Also, nearly identical bead spacing is noted for both flight and ground-based tests with the stainless steel specimens, while spacing on the tantalum specimens is larger for flight than for ground-based test. It is believed that the mechanism of vortex shedding is thus related to the beading pattern [14]. The discrepancies for the aluminum and tantalum are presently under further investigation.

E . DWELL SHAPE

Lack of hydrostatic pressure and dominance of surface tension will allow dwell pool shape to be different (more spherical) and may cause shallower eb penetration. The different pool shape will occur because surface tension acts to pull the melt toward cooler surfaces which is away from the electron beam in this case. Assuming that the net gravitational field is always aligned with the beam in Skylab processing, the situations illustrated in Figure 4 will result regarding bulk melt behavior of the dwell pool. As seen in Figure 4a surface tension dominance will pull the melt away from the beam, resulting in less resistance and deeper beam penetration than in terrestrial processing when heating from above. When heating from the side, however, terrestrial processing allows the melt to run out of the pool which will probably lead to even less resistance and more penetration than in space processing. Shallower dwell penetrations should be expected aboard Skylab because ground samples were processed as in Figure 4b.

As predicted, the gravity sag illustrated in Figure 4 was evident in the ground samples shown in Figures 5a and 6a which also lead to more extensive dwell penetration than in the flight samples. No "sag" was evident in the aluminum and steel flight samples shown in Figures 5b and 6b as the dwell shape appeared similar to Figure 4a.

F. SURFACE TENSION MEASUREMENTS

The surface tension of stainless steel was experimentally determined (Ref. 15). The resulting values for the estimated liquid/vapor surface energy are given below.

Temperature (^{o}K)	Surface Energy (10^{-5} N/m)	Liquid Density (gm/cc)
1868	1800	6.97
1943	1779	6.89
1993	1756	6.81
2058	1710	6.73

These values are adequate for engineering evaluation analysis. The absolute accuracy cannot be estimated, and no previous measurements have been found for comparison. The important temperature coefficient of variation of the surface energy for SS 304 alloy is rather large, -0.47 (x 10^{-5} N/m^{o}K) (erg/cm^{2}^{o}C).

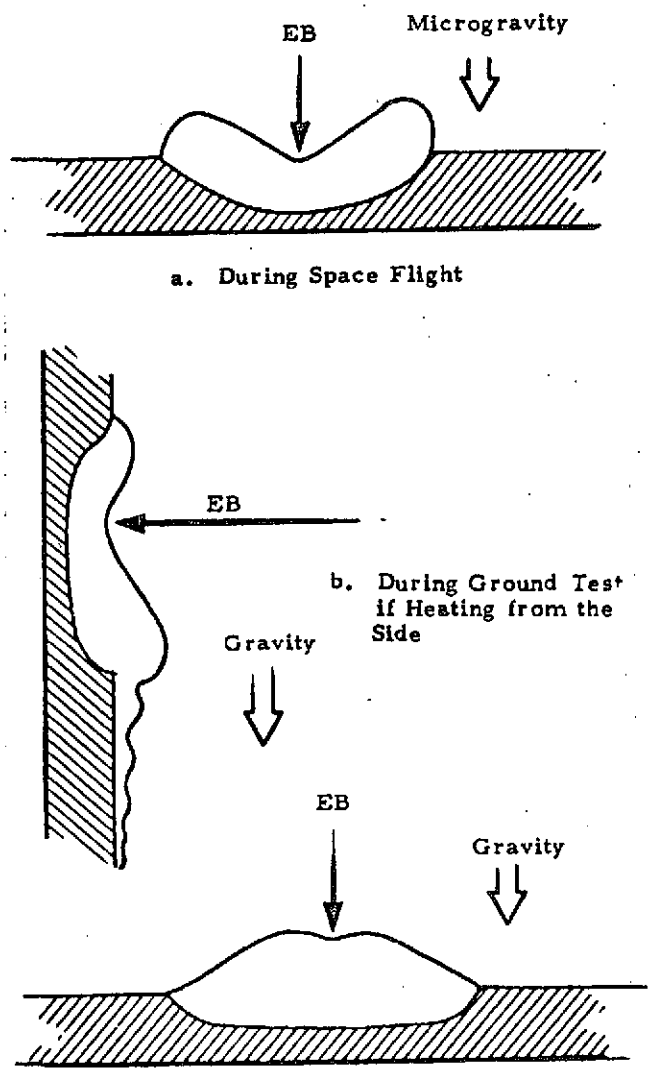

FIGURE 4. PROPOSED M551 DWELL POOL BEHAVIOR [17]

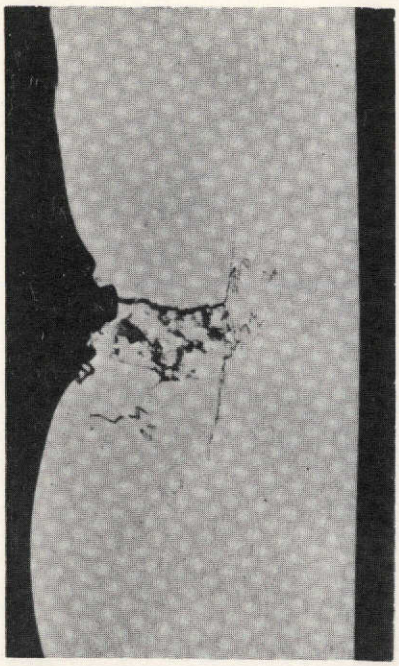

a. Ground (Gravity downward)

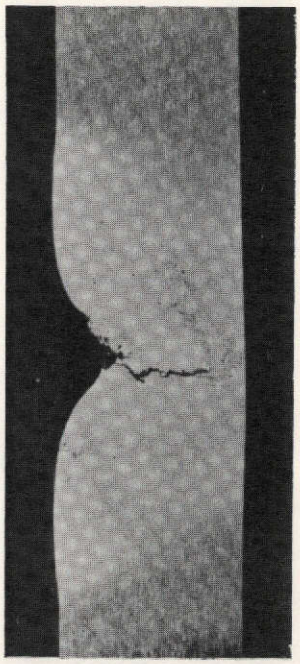

b. Flight (Microgravity)

Fig. 5 Cross section of aluminum dwell region

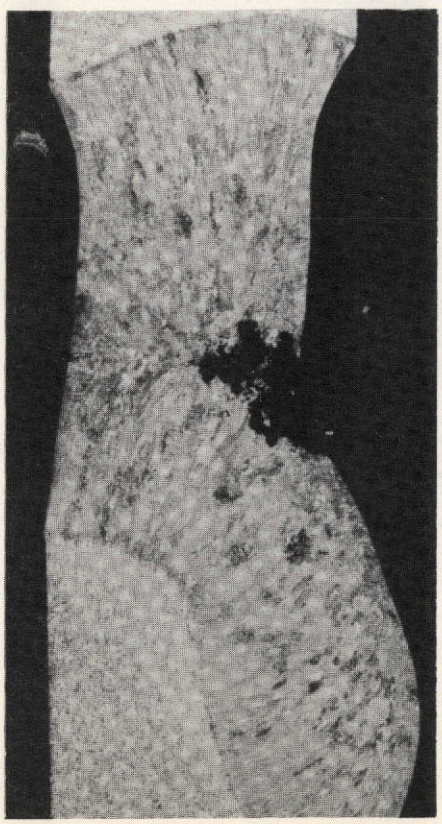

a. Ground (Gravity downward)

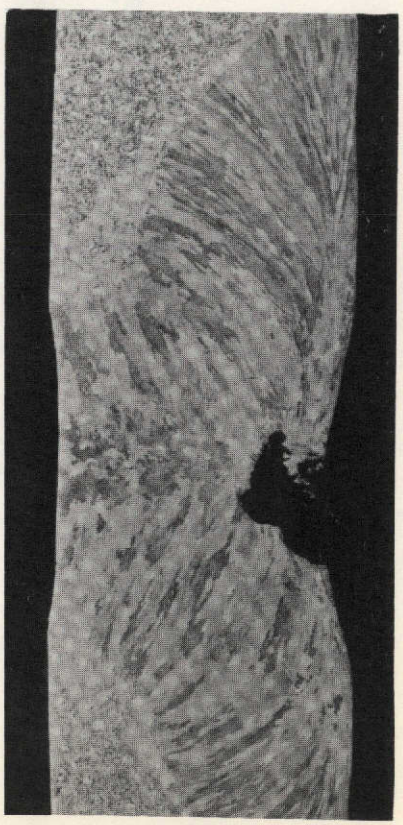

b. Flight (Microgravity)

Fig. 6 Cross section of stainless steel dwell region

G. CONCLUSIONS

The primary conclusion which can be reached from the results now available is that no significant practical differences exist between terrestrial and microgravity electron beam melting. The differences found to date — oxide free front surface for the full penetration weld in the aluminum flight samples and the lack of gravity sag and shallower penetration in the stainless steel flight sample dwell — do not seem to have any practical benefits or detriments for conducting this operation in space. Although no results have been reported to date, the change in spiking frequency with gravity level and degree of melt superheat could lead to an increase in porosity and cold shuts in low gravity electron beam welding.

It is noted that the only other known low gravity electron beam welding experiments ever conducted [16] have come to similar conclusions using similar materials, beam parameters, chamber and disks, movie coverage and low-g aircraft experimentation. Their conclusions [16] were that not much difference existed between Earth and low-g specimens; aluminum rendered continuous beading, whereas stainless steel resulted in droplet beading; weld shape and penetration were the same on Earth and in low-g; and more porosity existed in one of the low-g specimens.

No qualitative evaluations could be made on the magnitude and pattern of flow in the dwells because filming speed was too low. This was true for both ground and flight tests.

Surface tension and vaporization forces were dominant for this experiment both on the ground and in Skylab. Gravity forces were also important in determining dwell shapes for stainless steel and aluminum ground tests.

SECTION III. M552 EXOTHERMIC BRAZING EXPERIMENT

This section contains descriptions of the physical forces and their effect for the M552 experiment. The first portion of the chapter addresses the capillary flow analysis, while the second segment discusses bubble dynamics associated with M552. The next two sections discuss variable gap flow effects and pertinent surface tension measurements, respectively. Finally discussions of flight results are presented

The solid materials being brazed were tubular sections of 304L stainless steel and pure nickel. The brazing alloy was a eutectic composition mixture of silver and copper (72% silver, 28% copper) containing a small concentration (0.5%) of lithium. There were four specimen designs in which the most important variations were in the composition of the solid (stainless or nickel) and dimensions of the capillary gap between the inner tubular section and the concentric outer sleeve. In all specimens the silver-copper braze alloy was preplaced in ring-grooves situated for that purpose, one at each end of the specimen. Upon melting, flow of the liquid silver-copper alloy into the gap was under the impulsion of capillary action, in which the force producing flow is primarily surface tension. Gravity, when present, has a modifying effect on the surface tension force field which may or may not be negligible, depending on the magnitude of the capillary gap. The four specimen designs are listed below:

0.005" - Gap - 304L Material
SLS1 - Skylab Flight Specimen
MCS-1, 2 and 3 - Ground Characterization Specimens

0.010" - Gap - Pure Nickel
SLN2 - Skylab Flight Specimen
MCN-1, 2 and 3 - Ground Characterization Specimens

0.020" - Gap - 304L Material
SLS3 - Skylab Flight Specimen
MCS-4, 5 and 6 - Ground Characterization Specimens

0.000" - 0.030" Taper Gap - Pure Nickel Material
SLN4 - Skylab Specimen
MCN-4, 5 and 6 - Ground Characterization Specimens

A. CAPILLARY FLOW

The effect of gap width and low gravity on capillary flow in the M552 Exothermic Brazing Experiment has been studied. Time-to-spread, flow velocities and Reynolds number have been calculated for the configuration shown in Figure 7. The results are shown in Tables 4, 5 and 6.

The results indicate that [17]:

- Spreading time will be up to 50% shorter in gravity fields anticipated for Skylab than in ground tests.
- Turbulent or oscillatory laminar flow will occur in Skylab processing in certain gaps where only laminar flow could occur in ground tests.

The flow equation for an annulus is given by,

$$u = \frac{\rho g R^2 \phi}{8 \mu h} (h_o - h) \qquad \text{(III.1)}$$

where

u = velocity

h = axial position in annulus

ρ = density

R = sleeve radius

μ = viscosity

k = tube radius/sleeve radius

$$\phi = \frac{1 - k^4}{1 - k^2} + \frac{1 - k^2}{\ell n k}$$

g = gravity

$$h_o = \frac{2\sigma \cos\theta}{\rho g R (1 - k)}$$

σ = surface tension

θ = contact angle

Equation (III.1) was developed assuming laminar, steady state, incompressible, isothermal flow with $\vec{g}$ opposing the flow direction. It

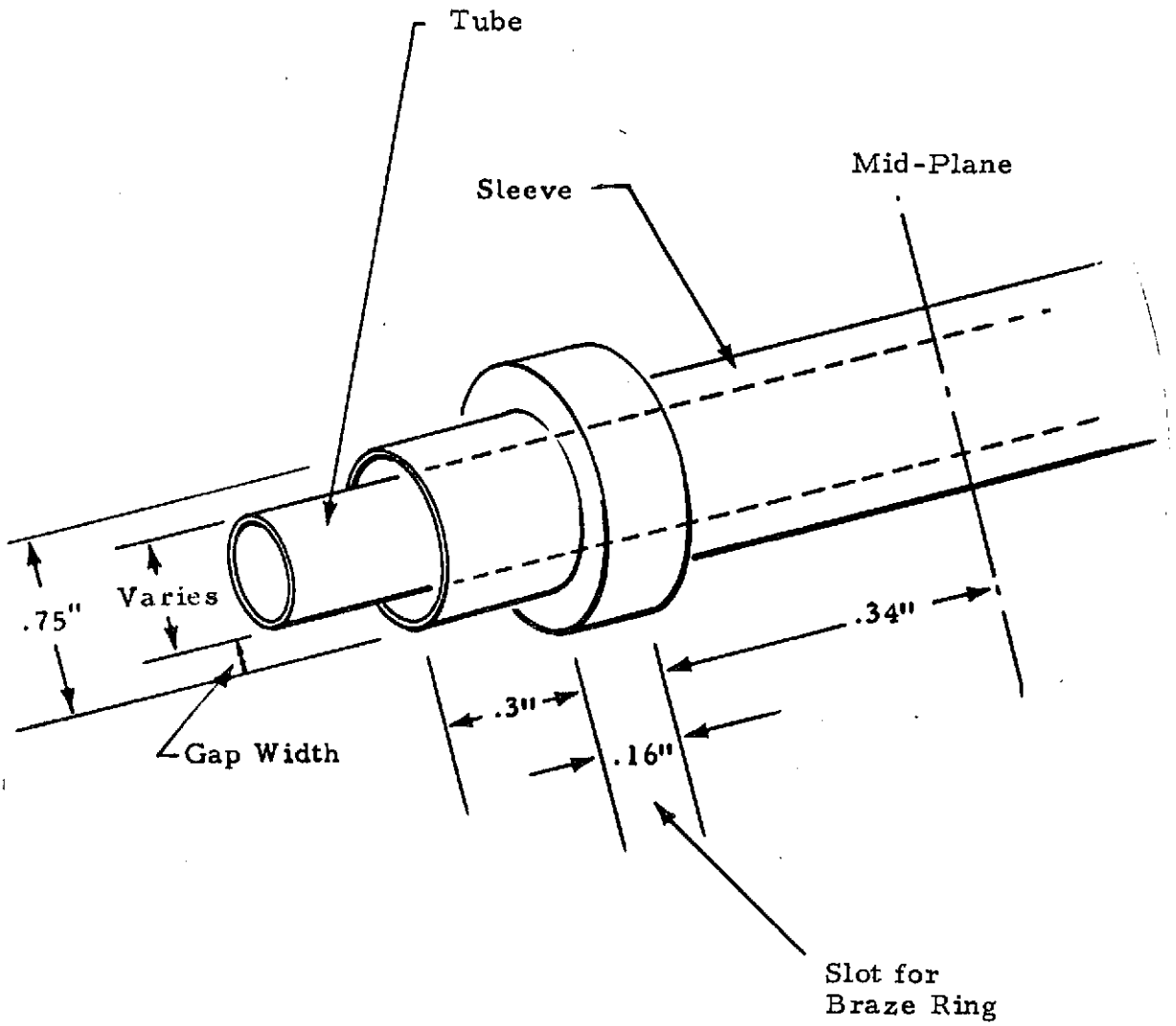

FIGURE 7. M552 CONFIGURATION

Table 4

M552 SPREADING TIMES

Gravity (g/g_E)	Gap Width (in.)	Spread Time (Annulus) (μ sec)
$2 \cdot 10^{-6}$	.005	12.00
	.010	6.00
	.020	2.97
	.030*	1.76
1	.005	13.60
	.010	7.47
	.020	4.42
	.030*	3.60

*Assuming no variation in gap width.

Table 5

M552 FLOW VELOCITIES

Geometry	Gravity (g/g_E)	Gap (in.)	Velocity (u) (cm/sec)
Annulus	$2 \cdot 10^{-6}$	.005	34
		.010	67
		.020	134
		.030*	200
	1	.005	30
		.010	55
		.020	90
		.030*	97
Slot	$2 \cdot 10^{-6}$	.005	33
		.010	66
		.020	132
		.030*	198
	1	.005	30
		.010	53
		.020	81
		.030*	84

*Assuming no variation in gap width.

Table 6

M552 REYNOLDS NUMBERS

Geometry	Gravity (g/g_E)	Gap (in.)	Re_1	Flow Regime
Annulus	$2 \cdot 10^{-6}$	.005	202	Laminar
		.010	794	Oscillatory
		.020	3200	Turbulent
		.030*	7210	Turbulent
	1	.005	182	Laminar
		.010	650	Laminar
		.020	2170	Oscillatory
		.030*	3490	Turbulent
Slot	$2 \cdot 10^{-6}$	.005	99	Laminar
		.010	395	Laminar
		.020	1580	Laminar
		.030*	3550	Turbulent
	1	.005	90	Laminar
		.010	315	Laminar
		.020	970	Laminar
		.030*	1500	Laminar

*Assuming no variation in gap width.

should be a valid approximation for the M552 configuration and processing conditions.

For very narrow gaps, Equation (III.1) reduces to that for flow in a slot which is given by

$$u = \frac{\rho g D^2}{12 \mu h} (h_o - h)$$

where

$$D = \text{slot width}$$

This equation was developed for assumptions similar to those of Equation (III.1) and will be just as rigorous except for geometrical effects.

The spreading time, t, for flow in an annulus can be given by

$$t = \frac{-8\mu}{\rho g R^2 \phi} (h_o \ell n (1 - h/h_o) + h)$$

Again, this equation is valid for isothermal, laminar, incompressible flow with $\vec{g}$ opposing flow. Levich [18] states it will only be an approximation if $t < \frac{\rho R^2}{\mu}$.

The Reynolds number for flow in an annulus is given as Reference 19,

$$Re_1 = \frac{2R (1-k) u\rho}{\mu}$$

or by Reference 20,

$$Re_2 = \frac{4R_H u\rho}{\mu}$$

where R_H = hydraulic radius.

The transition from laminar to turbulent flow occurs at $Re_2 \approx 2300$. The transition from laminar viscous flow to oscillatory flow is given by $Re_2 = 700$. By making the transformation, $k = 1 - \epsilon$, and allowing $\epsilon \longrightarrow 0$, it can be shown that $Re_1 \longrightarrow Re_2$ as $k \longrightarrow 1$. Thus the transition points for Re_1 are approximately 700 and 2300 also. The Reynolds number for flow in a slot is defined as

$$Re_s = \frac{\rho u D}{\mu}$$

and the laminar-turbulent transition is at $Re_s \approx 2000$.

B. BUBBLE DYNAMICS

Many ground and KC-135 aircraft tests for M552 have exhibited a bubble or void space within the braze structure. Analysis of the movement of such a bubble in low gravity and the nonisothermal conditions of M552 has been completed. These analyses are applicable to motion of gas bubbles only and will not predict the location of shrinkage voids.

Neglecting wall effects, the limiting velocity of a single bubble moving in a homogeneous liquid under the combined influence of a gravity field and a temperature gradient is given by Reference 21,

$$u = \frac{2}{3\mu_g B}\left[3\mu_g aA \frac{d\sigma}{dT}\frac{dT}{dz} - (\rho_g - \rho_\ell)\, ga^2 (\mu_g + \mu_\ell)\right]$$

where

$A = 2 + k_\ell/k_g$

$B = 3\mu_g + 2\mu_\ell$

k = thermal conductivity

μ = viscosity

a = bubble radius

σ = surface tension

T = temperature

ρ = density

g = gravity

and subscripts ℓ and g refer to the liquid and gas phases, respectively. The temperature gradient affects bubble motion through tangential stresses at the bubble-liquid interface. These stresses are caused by surface tension gradients across the bubble. The surface tension mechanism is termed the Marangoni effect, which can be caused by either temperature or concentration gradients.

The ratio of buoyant/Marangoni forces on the bubble is given by,

$$\gamma = \frac{(\rho_\ell - \rho_g)\, g\, a\, (\mu_g + \mu_\ell)\, A}{3\, \mu_g \frac{d\sigma}{dT} \frac{dT}{dz}}$$

where γ = buoyancy/surface tension forces. Values of γ for various size bubbles and gravity levels are given below for M552 conditions using a 10°C/cm temperature gradient,

Bubble Diameter (cm)	Gravity (g/g_E)	γ
10^{-4}	1	10^{6}
10^{-4}	10^{-6}	1
10^{-2}	1	10^{5}
10^{-2}	10^{-6}	10^{-1}

Thus, Marangoni forces will be important in Skylab, but not on ground tests.

C. CAPILLARY PUMPING IN TAPERED GAPS

Upon melting the braze alloy in the M552 tapered gap specimens (SLN-4, MCN-4, MCN-5 and MCN-6) will have the configuration shown in Figure 8. Ignoring gravity effects and contact angle hysteresis [22 and 23], the pressure gradients determining flow direction are determined solely by simple capillary effects, as follows [24, 25 and 26]:

$$P - P_1 = \frac{2\sigma \cos\theta}{R_1}$$

$$P - P_2 = \frac{2\sigma \cos\theta}{R_2}$$

where the contact angle θ, the pressures P, P_1 and P_2 and the radii of curvature R_1 and R_2 are shown in Figure 8. The term σ is the surface tension of the liquid vapor interface.

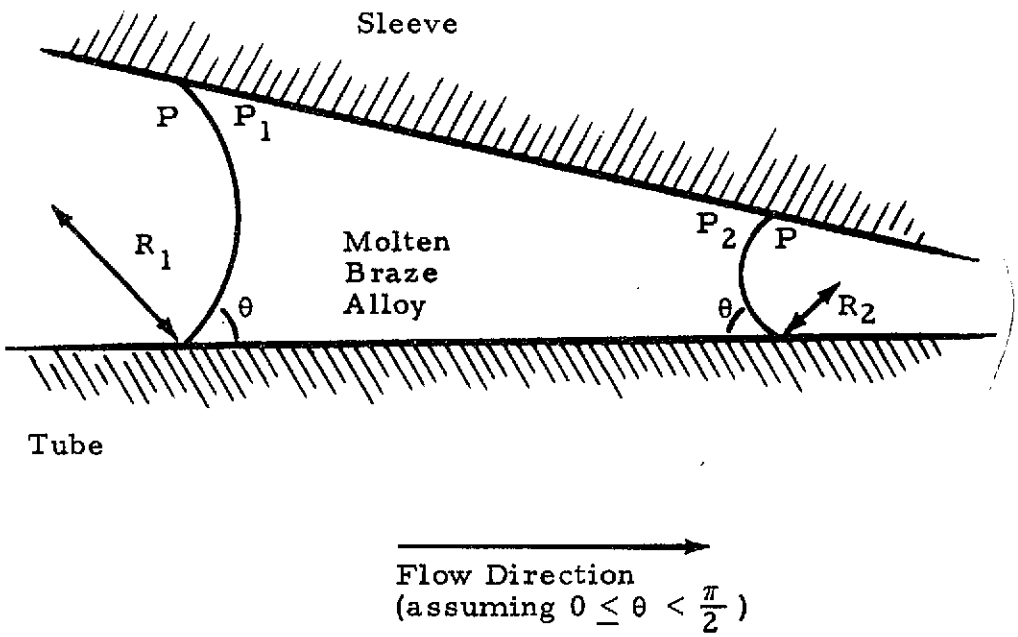

FIGURE 8. TAPERED GAP CAPILLARY PUMPING FOR THE M552 EXPERIMENT

By eliminating the common term P from these equations, the following results

$$P_1 - P_2 = 2\sigma \cos\theta \left(\frac{1}{R_2} - \frac{1}{R_1}\right) > 0$$

because R_1 is greater than R_2. Thus the molten braze will always flow toward the narrow end of the tube.

The same would be true when gravity is considered because ground tests were conducted vertically and g-levels aboard Skylab II were less than 10^{-4} g_E; i.e., the ratio of hydrostatic to capillary pressures are:

$$\frac{\rho g h}{2\sigma \cos\theta \left(\frac{1}{R_2} - \frac{1}{R_1}\right)} \leq 3 \times 10^{-3}$$

Like gravity effects, contact angle hysteresis (advancing and receding angles differ) should also have negligible effects on final melt position, because hysteresis will only affect the rate of flow and not the flow direction.

D. SURFACE TENSION MEASUREMENTS

The values of surface tension, σ, for both the Ag/Cu eutectic braze alloy BT720, and the same alloy with nominally 0.2% lithium addition, Lithobraze BT720, were measured as [15]:

	Temperature	Surface Tension
Braze BT720	1173°K	996 x 10^{-5} N/cm*
	1273	965
	1373	956
	1473	917
Lithobraze BT720	1273	967
	1413	942
	1473	930

*Multiply by 10^5 to get dynes/cm or ergs/cm^2

The surface energies of the two Ag/Cu braze alloys are plotted as a function of temperature in Figure 9. With an error of 1% in σ and 20°K in T, a least mean square line gives a slope of $S \cong d\sigma/dT$ = -0.25 x 10^{-5} N/cm°K (-0.25 ergs/cm^2°C). This can be compared with a value of S = -0.31 x 10^{-5} N/cm°K for pure copper.

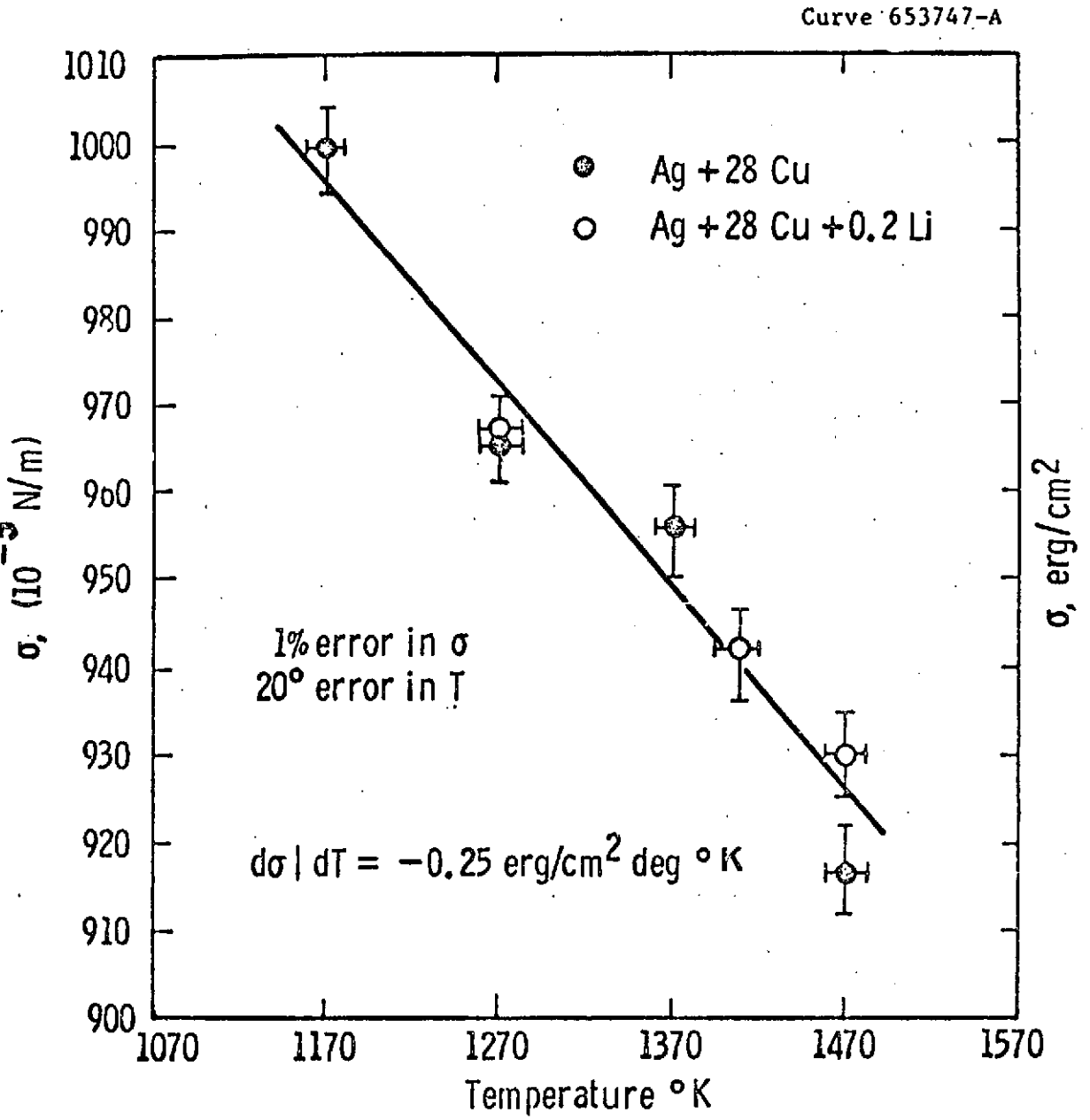

Fig. 9 –Surface energy vs temperature Ag-Cu solder alloys. Al_2O_3 substrate, argon atmosphere. [15]

E. FLIGHT RESULTS

Radioisotope tracer mapping of Skylab samples SLN-2 and SLN-4 showed very interesting differences and similarities when compared with similar maps of ground-test samples. One significant difference was the enhanced braze alloy flow (with subsequent increased movement of tracer alloy) observed in the samples brazed in space under near-zero gravity conditions. Radioactivity was observed for both samples SLN-2 and SLN-4 well outside of the ferrule region on the double-scribed or tracer pellet end. With gravitational forces absent, capillarity of surface forces were unopposed, resulting in rather dramatic increased flow of the braze alloy. Another difference due to the absence of gravity was manifested in sample SLN-4, a taper annulus sample, which demonstrated the absence of a braze "leveling" effect noted on ground-test samples; islands of braze alloy filled regions having very large gap widths. In some respects, the radiation intensity maps for the Skylab samples SLN-2 and SLN-4 were very similar to those obtained from earth samples. The tracer alloy moved initially toward the thermally hot regions near the igniters. The ^{110}Ag tracer maps for all of NASA M-552 braze assemblies suggest that such tracing can provide a picture of the thermal history for any particular assembly as well as accurate braze alloy flow information. Since no other analytical technique would provide this unique composite view of surface, gravitational, and thermal forces, radioisotope tracing proved useful in interpreting other metallurgical aspects of this experiment [27].

An observation of major importance is that true capillary flow can be developed in wide-gap apertures when gravity is absent. This had been predicted, and was a reason for inclusion of wide-gap specimens (SLS-3, 0.020 inch gap and SLN-4, tapering to 0.030 inch gap).

There are practical as well as scientific implications to wide-gap capillary behavior. One principal consequence is that brazing, as a means for joining materials, is a much more versatile process in zero gravity space environment than it is on earth. Commercial terrestrial capillary brazing is limited by gravity interference to gap clearances rarely exceeding 0.005 inch, which imposes serious constraints on machining and fixturing. The absence of the need for close clearances and relatively smooth parallel surfaces, as required on earth, greatly extends the applicability of brazing as contrasted, for example, with welding, fastening, or other joining techniques, when structural fabrication is to be done in space environment.

Some general characteristics of capillary flow were manifested in a review of metal distribution in all M552 Skylab specimens. The pressure in liquid near a small gap meniscus is smaller than near a wide gap meniscus; therefore pressure differences develop in complex

capillary systems tending to drive the liquid from wide gap to narrow gap locations. For example, when the braze gap was fairly narrow (SLS-1, 0.005 inch), the ring-grooves were almost drained of liquid; in a wide gap specimen (SLS-3, 0.020 inch), not only was the joint "starved" as mentioned above, but the wide gap was far less effective in draining liquid from the ring-grooves (thus contributing indirectly to the "starvation" of the joint). In consequence, an observable, measurable meniscus developed in ring-grooves near wide gaps. For example, the upper ring-groove in specimen SLN-4 is near a very wide (0.030 inch) gap, which was incapable of withdrawing much liquid from the groove and the residual liquid formed a meniscus according opportunity for observation of a radially symmetrical liquid-vapor surface contour in the absence of gravity. This contour has been found numerically consistent with the following equation which governs in the absence of gravity, provided the surface tension is uniform from point to point on the meniscus surface [28].

$$\frac{dY}{dX} = \sqrt{\left(\frac{\sigma}{\Delta P}\right)^2 \left(\frac{2Y}{y^2+C}\right)^2 - 1}$$

where

Y = distance from the centerline of the specimen to a point on the meniscus, measured perpendicular to the centerline

X = distance measured parallel to the centerline from the center of the ring-groove

C = integration constant

σ = surface tension

ΔP = pressure difference prevailing across the meniscus surface (and constant from point to point along the meniscus surface)

The conformance of the meniscus surface with the equation supports the conclusion that the liquid-vapor surface tension is substantially uniform. This is of importance because the surface tension is quite sensitive to variations in temperature and surface composition.

F. CONCLUSIONS

The absence of gravity greatly extends the scope of brazing, and, thereby, the applicability of brazing to fabrication in space. In zero

gravity environment, the surface tension forces begetting capillary flow are unfettered, while on earth these forces must compete with gravity. Study of braze alloy distribution in Skylab specimens clearly indicates that dimensional tolerances, especially braze gap clearances, will be far less critical to joining operations in space than on earth. The practical significance of this fact, which had been predicted but never tested, can hardly be overemphasized. In space fabrication, many joints, which on earth would be produced by welding, should probably be brazed.

Liquid-vapor boundary surfaces (menisci), and the flow of liquid metal under the impulsion of surface tension forces, are in close conformance with what had been predicted for zero gravity environment. There were no unexplained effects, and, in the Skylab specimens, the surface tension of liquid silver-copper alloy appears to have been quite uniform.

SECTION IV. M553 SPHERE FORMING EXPERIMENT

This chapter contains analyses of the physical forces for the M553 experiment. The first section contains analyses of the driving forces, magnitude and pattern of natural convective fluid flows which occur in the Sphere Forming Experiment. Following sections address trajectories of released samples, shape dynamics, surface tension measurements, shrinkage pressure in freezing spheres and flight results.

A. CONVECTION ANALYSIS

As in the other M512 experiments, the physical forces and attendant fluid dynamics of the M553 experiment are important factors in determining the quality of the final product. Flow patterns in the molten material are important because all of the sample materials have low entropies of fusion [1]. Thus, their solidification (microstructure) is controlled by the rate of heat transfer removal [2], which changes with the fluid flow [3 and 4]. The degree of flow will also determine the amount of mixing attained. If no or little flow were present, all heavier components would segregate to the lower portion of the spheres on earth, but to a negligible extent in the microgravity environment of space. Fluid flow can also affect the shape and release of the specimen while it is retained on the ceramic holder.

Application of dimensional analysis [5 and 6] to the governing equations for eb melting, coupled with ground-based and KC-135 experiments, should enable prediction of the extent of reduction or increase of motion in the molten metal and/or the change in flow pattern in electron beam melting in space. Possible physical forces which could induce fluid flow in the M553 experiment, and their causes, include:

- Effective Gravity Force: Resultant force on weld specimen due to earth's gravity and centrifugal and coriolis forces of orbiting spacecraft.
- Lorentz Force: Electromagnetic forces induced by passage of the electron beam current through the specimen.
- Electrostriction: Stresses induced when electrical permittivity changes with density.

- Magnetostriction: Stresses induced when permeability changes with density

- Electrostatic Force: Caused by presence of excess electrical charge (due to beam current and/or thermionic emission).

- Surface Tension: Tangential stresses at vapor-liquid interfaces can be induced if surface tension depends on temperature and/or concentration. Surface tension will also cause pressure gradients across curved interfaces.

- Density Differences Accompanying Phase Changes

- Beam Force: Impinging electrons giving up their momentum.

- Thermal Expansion: Dilation and compression of fluids whose density changes appreciably with temperature can induce fluid flow.

- Vibration: Uncontrolled movement due to engine operation, astronaut motion, particle impacts, etc.

- Centrifugal and Coriolis: Generated by disk rotation.

- Vapor Pressure: Evaporating molecules impart momentum which leads to normal stresses at vapor-liquid interface.

- Inertia Forces: Tend to sustain induced motions.

- Viscous Forces: Tend to resist driving forces.

Governing Equations

The preceding forces, which could influence fluid flow and solidification, appear explicitly in the following conservation equations which apply to formation of a molten pool by electron beam heating.

Continuity (Mass Balance):

$$\frac{\partial \rho}{\partial t} + \nabla \cdot (\rho \vec{V}) = 0$$

where

ρ = density

$\vec{V}$ = velocity vector

t = time

∇ = "grad" or "del" operator

Momentum:

$$\rho \frac{\partial \vec{V}}{\partial t} + \rho(\vec{V} \cdot \nabla)\vec{V} = -\nabla P + \mu \nabla^2 \vec{V} + \rho \vec{g}$$

Inertia Force | Viscous Force | Gravity Force

$$+ \vec{J} \times \vec{B} \qquad + \rho_e \vec{E}$$

Lorentz and Electromagnetostriction Forces | Electrostatic Force

where

P = pressure

μ = viscosity

$\vec{g}$ = gravity vector

$\vec{J}$ = electrical current density

$\vec{B}$ = magnetic flux density

ρ_e = excess charge density

$\vec{E}$ = electric field density

Energy:

$$\rho C_V \frac{\partial T}{\partial t} + \rho C_V (\vec{V} \cdot \nabla) T = k \nabla^2 T + \Phi + \rho Q$$

$$+ J_{c/\sigma'}^2 - (\beta T/K) \nabla \cdot \vec{V}$$

Thermal Expansion Source

where

T = temperature

C_V = heat capacity

k = thermal conductivity

Φ = viscous dissipation function

Q = internal heat sources

J_c = "conduction" current = $\sigma(\vec{E} + \vec{V} \times \vec{B})$

σ' = electrical conductivity

$$\beta = -\frac{1}{\rho} \left(\frac{\partial \rho}{\partial T}\right)_P$$

$$K = \frac{1}{\rho} \left(\frac{\partial \rho}{\partial P}\right)_T$$

Maxwell's Equations:

$$\nabla \times \vec{E} = -\partial \vec{B}/\partial t$$

$$\nabla \times \vec{H} = \vec{J} + \partial \vec{D}/\partial t$$

$$\nabla \cdot \vec{B} = 0$$

$$\nabla \cdot \vec{D} = \rho_e$$

where

$\vec{D}$ = displacement current

$\vec{H}$ = magnetic flux

Constitutive Relations:

$$\vec{D} = \epsilon' \vec{E}$$

$$\vec{B} = \mu' \vec{H}$$

$$\vec{J} = \sigma' (\vec{E} + \vec{V} \times \vec{B}) + \rho_e \vec{V}$$

$$\rho = \rho_o \left[1 - \beta \Delta T + K \Delta P \right]$$

where

ϵ' = permittivity (dielectric constant)

μ' = permeability

Vapor-Liquid Boundary Conditions:

Force Balance,

$$\underbrace{\left[P^{(2)} - P^{(1)} \right] n_i}_{\text{Beam and Vapor Pressure Forces}} + \underbrace{\frac{\partial \sigma}{\partial X_i} + \sigma \left[\frac{1}{R_1} + \frac{1}{R_2} \right] n_i}_{\text{Surface Tension Forces}}$$

$$= \left[\mu^{(2)} \left(\frac{\partial v_i^{(2)}}{\partial X_k} + \frac{\partial v_k^{(2)}}{\partial X_i} \right) - \mu^{(1)} \left(\frac{\partial v_i^{(1)}}{\partial X_k} + \frac{\partial v_k^{(1)}}{\partial X_i} \right) \right] n_k$$

where $P^{(1,2)}$, $\mu^{(1,2)}$, $v_i^{(1,2)}$, $v_k^{(1,2)}$ are, respectively, the pressures, viscosities, and velocity components in Phases 1 and 2, σ is the surface tension, R_1 and R_2 are the principal radii of curvature of the surface, $n_i (i=1, 2, 3)$ are the components of the unit vector normal to the surface and directed into the interior of Phase 1, and summation over a repeated index $(k=1, 2, 3)$ is assumed. (See [14] for details.)

Energy Balance,

$$\epsilon \sigma (T_s^4 - T_\infty^4) - k \vec{n} \cdot \nabla T_s = Q_{EB}$$

where

ϵ = emissivity

σ = Boltzmann's constant

T_s = surface temperature

T_∞ = environment temperature

$\vec{n}$ = outward unit normal vector to free surface

Q_{EB} = heat flux from electron beam

Continuity of Velocity,

$$\vec{n} \times (\vec{V}^{(1)} - \vec{V}^{(2)}) = 0$$

$$\vec{n} \cdot \vec{V}^{(1)} = \vec{n} \cdot \vec{V}^{(2)} = 0$$

Solid-Liquid Boundary Conditions:

Along stationary interfaces the no-slip condition (all components of velocity vanish) holds; whereas at moving interfaces (along melting or freezing fronts), a one-dimensional material balance yields

$$u_i = (1 - \rho_s/\rho_L)\, d\delta/dt$$

where

u_i = fluid velocity normal to the interface

δ = position of the interface relative to the origin of the spatial coordinate system

ρ_s = solid density

ρ_L = liquid density

This is the source of the density-difference-accompnahing-phase-change force for fluid flow. Also for a melting interface, an energy balance yields:

$$-k\nabla (T_L - T_S) = \rho_s \lambda \frac{d\delta}{dt}$$

where

T_L = liquid temperature at the interface

T_S = solid temperature at the interface

λ = heat of fusion

and

$$T_S = T_M$$

The preceding equations are based on the following assumptions:

- No influence of external fields on physical properties
- No coupling between constitutive flux relations (e.g., no Soret effect)
- Single-component, Newtonian fluid
- Constant physical properties
- Bulk coefficient of viscosity vanishes.

They are written in general vector form wherever possible, since they also apply directly to M551. It should be noted that only the differences in physical properties and geometry will differ in a dimensional analysis of M551 versus M553.

Dimensional Analysis

The controlling physical forces can be determined by nondimensioning each of the preceding equations and performing an order-of-magnitude comparison on the various dimensionless groups which result [5 and 6]. The key to successful analysis is in choosing the proper reference values; i.e., since no freestream velocity exists, which forces do we equate to estimate a "characteristic" or "typical" velocity. Choosing the proper characteristic velocity is very important, since the reference time, temperature, etc. usually depend on this velocity.

Previous examinations of film showing both KC-135 flight experiments and ground tests for the M553 experiment indicated fluid velocities exceeded 300 cm/sec (p. B-5 of Reference 29). Continued M553 film analysis has since shown that flow velocities for nickel

specimens on both KC-135 and ground tests have been approximately 20 cm/sec. Of the 14 possible forces affecting electron beam melting [30], only those shown in Table 7 yield characteristic velocities of this order of magnitude. These driving forces consist of couplings involving surface tension, gravity or Lorentz (electromagnetic) forces with inertia forces. Previous studies based on faster velocities had indicated coupling with viscous, rather than inertia, forces as controlling [29]. This indicates the importance of choosing the correct characteristic velocity. Preliminary analysis also suggests that magnetostriction forces may also be important, but gross uncertainty in electromagnetic property data for liquid metals precludes any decision at the present time.

Table 7

PROBABLE CHARACTERISTIC VELOCITIES IN ELECTRON BEAM MELTING

Controlling Forces	Velocity	
	Functional Form	Value (cm/sec) for Nickel in M553
Inertia = Surface Tension	$(ST/\rho L)^{1/2}$	20
Inertia = Lorentz	$(\sigma' E^2 L/\rho)^{1/3}$	1
Inertia = Gravity	$(gL)^{1/2}$	18 at $1\ g_E$ 6 at $10^{-4} g_E$
Viscous = Lorentz	$(\sigma' E^2 L^2/\mu)^{1/2}$	7

The dimensionless momentum equation which determines fluid flow in electron beam melting becomes (upon choosing the surface tension-inertia characteristic velocity),

$$\frac{1}{N_{St}} \rho \frac{\partial \overline{V}}{\partial t} + \frac{1}{N_{Oh}} \rho (\overline{V} \cdot \nabla) \overline{V} = - \frac{1}{2N_{Oh}} \nabla P + \nabla^2 \overline{V}$$

$$+ \frac{N_{Bo}}{N_{Oh}} (\rho \overline{g}) + \frac{2N_{MI}}{N_{Oh}} (\overline{V} \times \overline{B}) \times \overline{B} \qquad \text{(IV.1)}$$

where

N_{St} = Stokes number = $\mu t_o / \rho_o L$

= duration of process/residence time

N_{Oh} = Ohnesorge number = $\mu / \sqrt{\rho_o L S T_o}$

= viscous force/surface tension force

N_{Bo} = Bond number = $\rho_o g_o L^2 / S T_o$

= gravity force/surface tension

N_{MI} = Magnetic interaction number = $\frac{B_o^2 L}{2\mu_o' S T_o}$

= magnetic force/surface tension

Using physical property data for nickel and beam parameters for the M553 experiment, the equation reduces to

$$10^3 \rho \frac{\partial \overline{V}}{\partial t} + 10^3 \rho (\overline{V} \cdot \nabla) \overline{V} = - 10^3 \nabla P + \nabla^2 \overline{V}$$

$$+ G(\rho \overline{g}) + 10^{-1} (\overline{V} \times \overline{B}) \times \overline{B}$$

where

$G = 10^3$ for earth gravity

$G = 10^{-1}$ for expected Skylab gravity.

This order-of-magnitude analysis indicates that surface tension driven convection will occur both in ground tests and for Skylab conditions because $N_{Oh} << 1$. This is confirmed by KC-135 M553 tests. Furthermore, gravity driven convection will exist on ground tests, but will be negligible in the reduced gravity of Skylab. Thus different forces will

control convection on earth versus Skylab. The preceding analysis also indicates that electromagnetic or Lorentz forces will be negligible with regard to causing fluid motion.

The surface tension driving force considered above is actually a surface tension gradient caused by radial and lateral temperature gradients. Ignoring convection, gradients of at least several hundred degrees Celsius per centimeter have been predicted during melting [31]. It can be shown by dimensional analysis (equate inertial and viscous terms) that the motion caused by the initial temperature gradients will occur in less than 0.1 second and can persist for 60 seconds after removing the driving force. This means that there will be some fluid motion during solidification if the M553 specimens freeze after 30 to 40 seconds as predicted.

Values of the pertinent dimensionless groups for the remaining M553 materials are given in Table 8. As can be seen, no significant changes are evident from the preceding conclusions for pure nickel.

Table 8

M553 DIMENSIONAL ANALYSIS

Material	N_{Oh}	N_{Bo}	$\frac{1}{N_{Oh}}$	$\frac{N_{Bo}^{*}}{N_{Oh}}$	$\frac{N_{Bo}^{\dagger}}{N_{Oh}}$
Ni-Sn	4.4×10^{-4}	1.50	2292	3437	.34
Ni-Ag	5.0×10^{-4}	1.53	1991	3043	.30
Ni-Cu	4.45×10^{-4}	1.54	2107	3241	.32

*With Earth gravity (9.8 m/sec^2)

†With 10^{-4} Earth gravity

It should also be mentioned that the effects on fluid motion of surface free charges (excess electrostatic charge) and related electric and magnetic forces at the drop surfaces have been examined. The results of the examination indicate that these surface charges are negligible driving forces for fluid motion. These results were also reviewed by

Professor J. R. Melcher of MIT's Electrical Engineering Department, and he was in full agreement with these results*. Furthermore, from the manner in which patches of surface contaminants moved about in the ground films, it is apparent that surface tension driven flows due to concentration gradients are also important in this experiment. No reliable data exist, however, on what these impurities are, nor what the value of surface tension gradient with composition is. Thus the Marangoni effects are limited to thermal differences only in this study.

B. M553 TRAJECTORY ANALYSIS

One of the most important aspects of the M553 experiment is the motion of the sphere after deployment since this determines what free-float time will exist. In order to predict the motion, a trajectory program has been developed that includes allowances for:

- Electron beam force
- Deployment velocity (spring)
- Vaporization force based on 3-D temperature history
- Skylab orbit considerations
- M512 position considerations, and
- Allowances for additional forces as independent subroutines (KC-135 g-level data).

In general a solution to the equation of motion

$$\frac{d^2\vec{R}}{dt^2} = \vec{f}\,(t)$$

is obtained numerically via Simpson's rule subject to the following boundary conditions:

$$\vec{R} = 0 \text{ and } \frac{d\vec{R}}{dt} = \vec{V}_o \text{ at } t = 0$$

Integration of the equation of motion twice yields

$$\vec{R} = t\,\vec{V}_o + \int_0^t \int_0^\eta \vec{f}\,(\xi)\, d\xi\, d\eta$$

*Private Communication, Huntsville, Ala., 11 June 1973.

which produces the desired trajectory in chamber coordinates centered on the specimen. This computed trajectory is then transformed to camera coordinates to show the path as seen in the film, i.e.,

$$\vec{R}'(t) = \left[A\right] \vec{S}(t)$$

where $\vec{R}'(t)$ is the projected trajectory and $\left[A\right]$ is the transformation matrix obtained from the hardware. For camera 1

$$A = \begin{bmatrix} .932 & -.363 & 0 \\ -.203 & -.521 & -.829 \\ .301 & .773 & -.560 \end{bmatrix}$$

and for camera 2

$$A = \begin{bmatrix} .661 & -.183 & -.728 \\ -.224 & -.974 & .041 \\ -.716 & .136 & .685 \end{bmatrix}$$

The eb force was discussed in Reference 31 and Table 9 gives the magnitude of this force for two eb currents. To establish the motion as a result of the eb force, the conversion efficiency and eb cutoff time must be known. This time corresponds to the time delay associated with automatic shutdown of the eb due to sting melting. Original estimates were from 10 to 20 milliseconds; however, high speed movies (1000 frame/sec) taken during the M553 ground-based test at MSFC on 20 October 1972 show conclusively that longer times exist. During their test the spring loads were varied on the shutdown mechanism to experimentally establish the time interval the eb is on after melting occurs. It was found that for a 150-g spring load a cut-off time of 410 milliseconds was measured while 220 milliseconds were observed for a 200-g load. This cutoff time translates into a free-float time of approximately 12 seconds for a 150-g load and 23 seconds for the 200-g load. Thus the expected free-float time is drastically reduced from the 250 seconds corresponding to the original 20 milli-seconds estimate.

An analysis was performed to determine if the cohesive energy-generated kinetic energy is sufficient to cause deployment in the absence of external forces. This was done to allow initial conditions to be calculated. To reduce the complexity of the problem, the following assumptions were made:

Table 9

TOTAL FORCE DUE TO ELECTRON BEAM

$$F_e = I \sqrt{\frac{2 m_e V}{e}}$$

I (amp)	e (coulomb)	m_e (kg)	V (V)	F_e (N)	F_e (dyne)
0.05	$1.6(10)^{-19}$	$0.9(10)^{-30}$	$2(10)^4$	$2.38(10)^{-5}$	2.38
0.10	$1.6(10)^{-19}$	$0.9(10)^{-30}$	$2(10)^4$	$4.76(10)^{-5}$	4.76

- Zero gravity field
- No sting melting
- Sting pulled down before breaking
- Perfectly spherical free surface, and
- Contact angle of 120 degrees.

An energy balance was made between the initial and final states and from this the kinetic energy is found as

$$KE = \sigma_{LV} \left(A_{LV}^{(i)} - A_{LV}^{(f)} \right) + \sigma_{LS} \left(A_{LS}^{(i)} - A_{LS}^{(f)} \right)$$

This kinetic energy was calculated as a function of penetration (H) of liquid into orifice. The value of H simulates the effect of the spring in pulling the liquid down via adhesion between liquid and solid sting. The results of this calculation are

Penetration, H (cm)	Kinetic Energy (ergs)
0.0	0.0
0.1	62.7
0.5	293.0
1.0	597.0

The value of the kinetic energy must then be greater than the work of adhesion (or energy of adhesion) for deployment to occur. The work of adhesion was found to be 265 ergs; thus for depressions of more than 0.5 cm deployment will occur due to cohesive effects alone. These criteria are included in the trajectory computer program to allow initial conditions for the numerical integration to be determined.

Tables 10 and 11 show the surface temperature distribution at 3.0 and 3.5 seconds, respectively, for Ni and Ni-12% Sn. These data were used in conjunction with the Langmuir theory discussed in Reference 31 to calculate the net vaporization force as a function of time. A sample calculation is presented in Table 12 for both Ni and Ni-12% SN for the first second after eb cutoff. It is seen that between 3.5 and 4.25 seconds the vaporization force is of the same order of magnitude as the eb momentum force. During the first half second the calculations yield a large vaporization force (comparable to surface tension forces) and represent an intolerable situation as far as the free-float time is concerned. However, due to the large temperature gradients existing, the resulting surface tension driven convection will tend to reduce these values.

The Skylab orbit effects are included in the analysis by the method of Parker and Gatewood [32]. The computer program presented in Reference 31 was used as a subroutine in the present analysis to couple the effects of M512 position and orbit to the physical phenomena occurring in the vacuum chamber.

C. CONCLUSIONS BASED ON TRAJECTORY COMPUTATIONS

It has been shown that free-float times from 32 to 48 seconds (depending on the material) are required for complete containerless solidification to occur. The magnitude of each of the physical forces was discussed and general comments made concerning the effect of each on free-float time in the previous section. This subsection summarizes some of these conclusions.

TABLE 10

TEMPERATURE DISTRIBUTION AT 3.0 SECONDS

Node No.	Nickel		Nickel – 12% Tin	
	Temp. (°C)	Vapor Pressure (mm Hg/cm^2)	Temp. (°C)	Vapor Pressure (mm Hg/cm^2)
36	2036	.3959	2013	.7001
37	1463	.0006	1537	.0069
38	2193	.464	2157	.6965
39	1900	.0395	1903	.0962
40	1728	.0067	1757	.0253
41	1677	.0037	1716	.0168
42	1677	.0037	1716	.0168
43	1728	.0067	1757	.0254
44	1900	.0400	1903	.0963
45	2193	.4644	2157	.6965
46	1801	.0202	1815	.0602
47	1695	.0063	1731	.0266
48	1609	.0022	1663	.0132
49	1573	.0014	1634	.0096
50	1573	.0014	1634	.0096
51	1609	.0022	1663	.0132
52	1695	.0063	1731	.0266
53	1801	.0201	1815	.0602
54	1633	.0030	1680	.0159
55	1584	.0016	1642	.0105
56	1537	.0009	1605	.0069
57	1513	.0006	1586	.0056
58	1513	.0006	1586	.0056
59	1537	.0009	1605	.0069
60	1584	.0016	1642	.0105
61	1633	.0020	1680	.0158
62	1535	.0006	1602	.0049
63	1515	.0005	1585	.0041
64	1492	.0003	1567	.0033
65	1480	.0003	1557	.0030
66	1480	.0003	1557	.0030
67	1492	.0003	1567	.0033
68	1515	.0005	1585	.0041
69	1535	.0006	1602	.0049

TABLE 11

TEMPERATURE DISTRIBUTION AT 3.5 SECONDS

Node No.	Nickel		Nickel-12% Tin	
	Temp. (°C)	Vapor Pressure (mm Hg/cm^2)	Temp. (°C)	Vapor Pressure (mm Hg/cm^2)
36	1689	.01249	1678	.0332
37	1601	.00429	1624	.0185
38	1685	.0041	1676	.0111
39	1679	.0038	1674	.0109
40	1672	.0035	1671	.0105
41	1667	.0033	1670	.0103
42	1667	.0033	1670	.0103
43	1672	.0035	1671	.0105
44	1679	.0038	1674	.0109
45	1685	.0041	1676	.0111
46	1675	.0050	1672	.0144
47	1668	.0046	1669	.0140
48	1658	.0041	1665	.0135
49	1652	.0038	1662	.0131
50	1652	.0038	1662	.0131
51	1658	.0041	1665	.0135
52	1668	.0046	1669	.0140
53	1675	.0050	1672	.0144
54	1657	.0040	1663	.0131
55	1651	.0037	1660	.0128
56	1642	.0033	1657	.0123
57	1636	.0031	1654	.0200
58	1636	.0031	1654	.0200
59	1642	.0033	1657	.0123
60	1651	.0037	1660	.0128
61	1657	.0040	1663	.0131
62	1634	.0022	1649	.0083
63	1630	.0021	1648	.0082
64	1624	.0020	1645	.0080
65	1621	.0019	1644	.0078
66	1621	.0019	1644	.0078
67	1624	.0020	1645	.0080
68	1630	.0021	1648	.0082
69	1634	.0022	1649	.0083

Table 12

SUMMARY OF VAPORIZATION FORCE CALCULATION

Vaporization Force (dynes)	Time (sec)					
	3.00	3.25	3.50	3.75	4.00	4.25
Nickel						
f_x	882	55	8	1.5	0.3	.07
f_y	1480	126	25	5.8	1.3	.3
f_z	292	25	5	1.0	0.25	.06
Nickel-12% Tin						
f_x	1400	102	9	1	0.16	.02
f_y	2470	240	41	6	1.0	.16
f_z	485	47	8	1	0.2	.03

- Electron beam force for a 460-g spring load has a duration of approximately 100 milliseconds and gives rise to a float time of 40 seconds.
- Kinetic energy of sphere due to spring effects (deployment technique) gives rise to float times of greater than 50 seconds.

- Vaporization force produces float times that are probably the critical link in process. Best estimates of the corresponding float time between 1/4 second after eb cutoff and occurrence of an isothermal outer layer range from 5 to 20 seconds. For some cases the time could even be considerably less than 5 seconds.

- Skylab orbit effects give rise to 29 to 46 seconds of float time.

- Superposition of all of these forces produces an additive (as opposed to canceling) effect in most cases. Trajectory calculations show that even with conservative vaporization forces float times of less than 15 seconds will occur.

Lockheed documented in December 1972 [33] an early projection of anticipated float times less than the required containerless solidification times and again in April via the Science & Engineering Information Technical Note [34]. In the latter report a conservative estimate of less than 20 seconds was forecast.

Another potential problem area, discussed in the 27 March 1973 presentation at MSFC, is that even with the relatively large forces on the sphere during the critical time of deployment, the possibility of "sticking" exists. Films of the KC-135 flight test showed that an adherence to the ceramic occurs on occasion that finally results in deployment due to acceleration transients in the ballistics trajectory of the aircraft. A typical sequence is shown in Figure 10. The events are referenced to the time corresponding to what appeared to be the fully molten condition, t=0. For the ensuing 0.300-second, that adherence to the ceramic occurred with periodic motion due to the acceleration transients is evident in the film sequence. At 0.310-second, deployment occurred with the trajectory shown in Figure 10. The important point remains, however, that without the acceleration transients (relatively large compared to the Skylab gravitational environment) specimen retention could have occurred. This adhesion is probably due to contamination of the ceramic from previous melts. The conclusion is that the possibility of unintentional retained specimen may occur in the actual Skylab mission.

D. SHAPE DYNAMICS

This subsection presents a summary of calculations made for Ni and Ni-12% SN based on the thoughts outlined in Reference 31. First, the formation times are shown in Table 13 where it is seen that the transformation to minimum energy occurs very rapidly. However, due to inertial considerations, the spherical free surface is

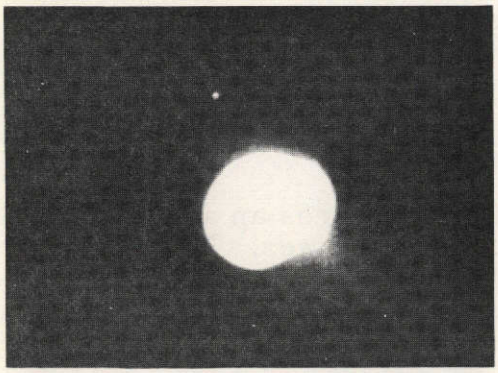

t = 0 (sec)

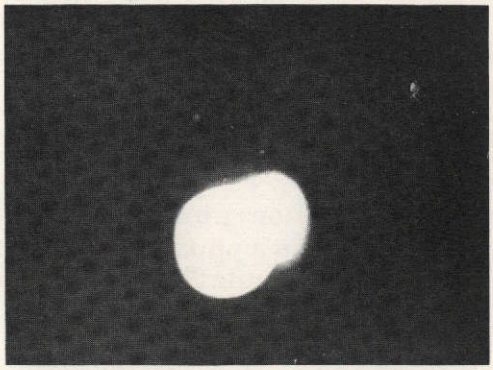

t = .250 (sec)

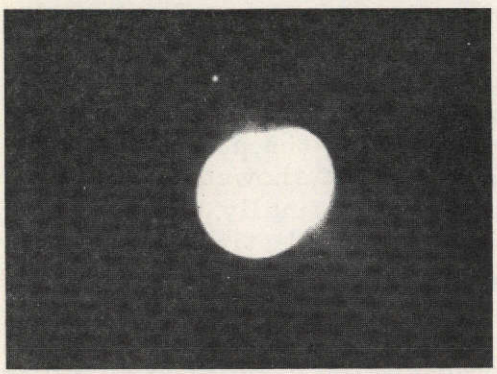

t = .275 (sec)

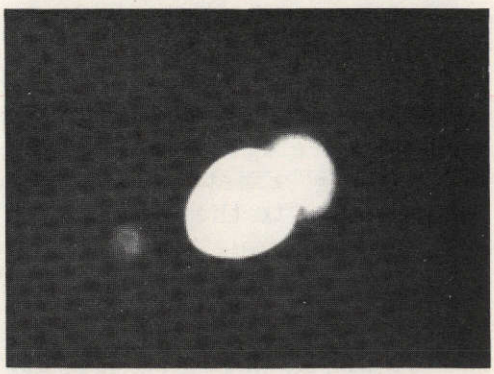

t = .290 (sec)

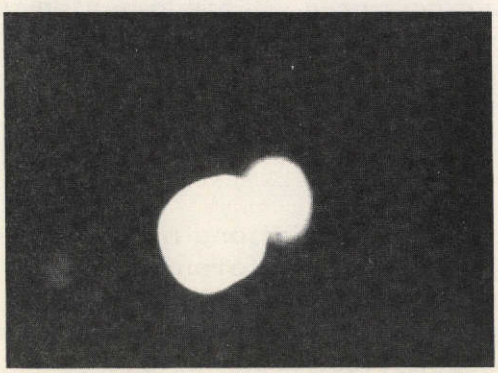

t = .295 (sec)

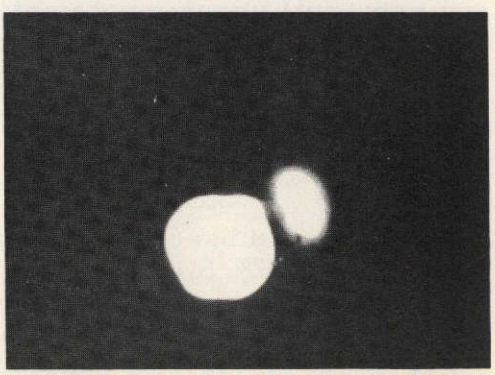

t = .310 (sec)

FIGURE 10. TRAJECTORY SEQUENCE – MARCH 1972 KC-135 FLIGHT (NICKEL) (CONTINUED)

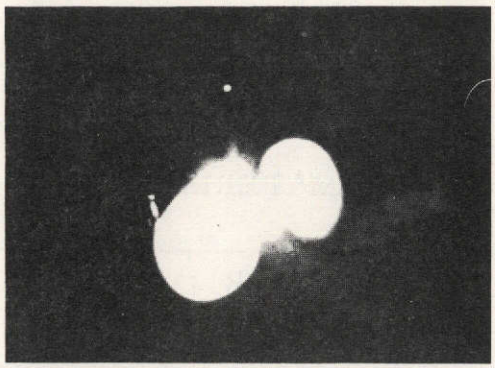

t = .325 (sec)

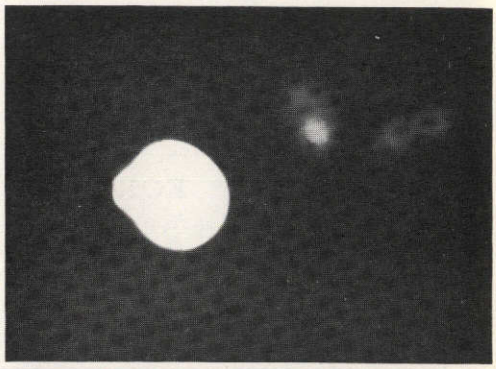

t = .360 (sec)

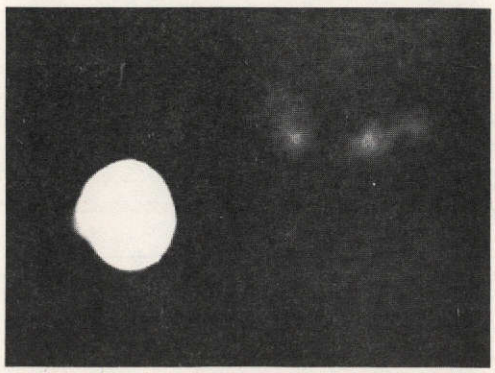

t = .395 (sec)

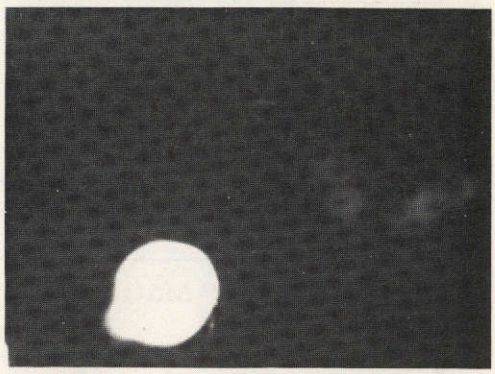

t = .400 (sec)

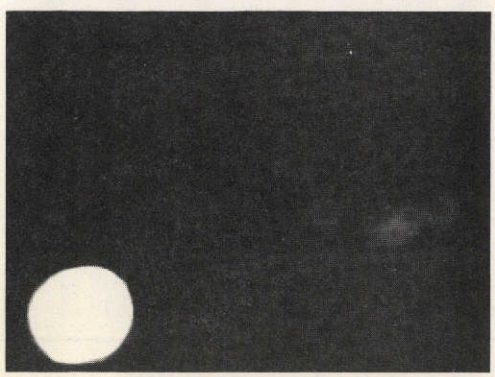

t = .450 (sec)

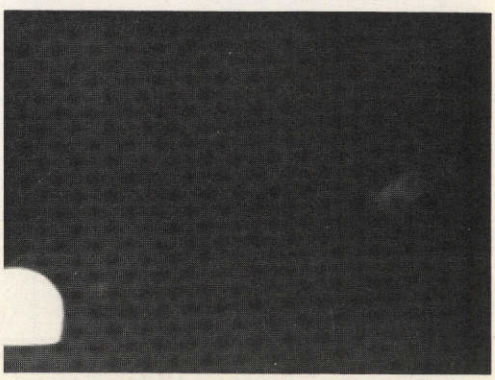

t = .515 (sec)

FIGURE 10. TRAJECTORY SEQUENCE (CONCLUDED)

"overshot" and oscillations are set up which continue until dissipated by viscous damping. Table 15 gives the oscillation frequencies while Table 14 shows the time required for viscous effects to dampen an initial perturbation to 0.01% and 1% of its initial value.

Table 13

FORMATION TIMES FOR M553 MATERIALS

M553 Materials	ρ (g/cm^3)	σ (dyne/cm)	R (cm)	T (sec)
Ni	7.85	2050	.3175	.011
Ni-12% Sn	7.80	1500	.3175	.013

Table 14

FREQUENCY FOR M553 MATERIALS

Material	Frequency (Hz)
Ni	41
Ni-12% SN	35

Table 15

DECAY TIME FOR M553 MATERIALS

Material	μ (g/cm-sec)	ρ (g/cm^3)	R (cm)	Time (constant)	Time (.01%)	Time (1%)
Ni	.05	7.85	.3175	3.14	28.8	14.5
Ni-12% Sn	.043	7.80	.3175	3.62	33.0	16.7

E. SURFACE TENSION MEASUREMENTS

The values of σ_{LV}, θ, and W_A determined from sessile drop experiments [15] are given in Table 16.

Table 16

WORK OF ADHESION (W_A) FOR NICKEL AND ITS ALLOYS ON $A\ell_2O_3$ (x 10^{-5} N/cm)

	Temp. (^oK)	σ_{LV}	θ (deg)	W_A
Nickel	1773	1719	135	503
	1973	1676	137	450
	2068	1659	(113)	(1011)
Ni-1% Silver	1793	1637	135	479
	1983	1586	136	445
	2138	1564	128	601
Ni-12% Tin	1683	855	130	305
	1983	806	133	256
	2093	782	130	279
Ni-30% Copper	1743	1506	126	621
	2003	1468	130	524
	2073	1411	133	449

F. SHRINKAGE FORCES

When spherical melts solidify, the innermost melt is the last to freeze. The advancing outer solid shell leads to hydrostatic tensions, even negative pressures, in the residual liquid and the general plastic collapse of the spherical casting. The contraction (about 3% for most metals) is caused by solidification shrinkage. Several recent analyses have been performed for this configuration [35 through 37], and two extreme cases which could exist are shown in Figures 11 and 12. In Figure 11 the residual liquid is considered to have undergone cavitation. The homogeneous fracture pressure of most liquid metals is thought to be on the order of -10^{-5} atm; however, heterogeneous nucleation may be possible at less negative pressures.

The tensile pressures within the residual liquid can be calculated assuming various growth rates and outer shell deformation modes: elastic-plastic, Bingham, viscous or creep flow. Using the creep flow model, negative pressures in the liquid core of 1 cm radius nickel sphere are shown in Figure 13 using initial pressure of 1 atm. Nickel

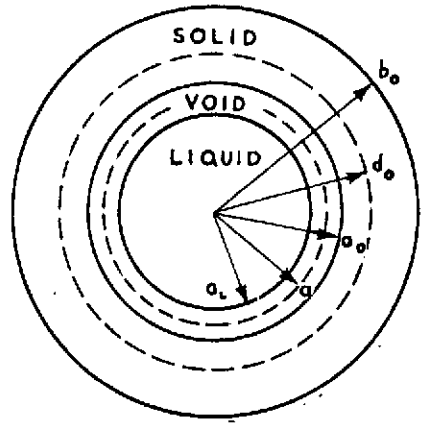

FIGURE 11 . UNSTRAINED OUTER CASTING AND HOMOGENEOUS NUCLEATION OF RESIDUAL LIQUID UNDER EXTREME NEGATIVE PRESSURES [35]

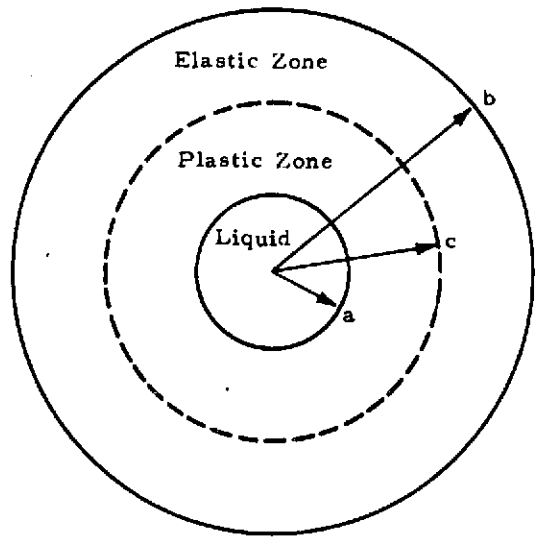

FIGURE 12 . STATE OF A SOLIDIFYING SPHERICAL CASTING WITH EXTERIOR SHELL DEFORMATION [35]

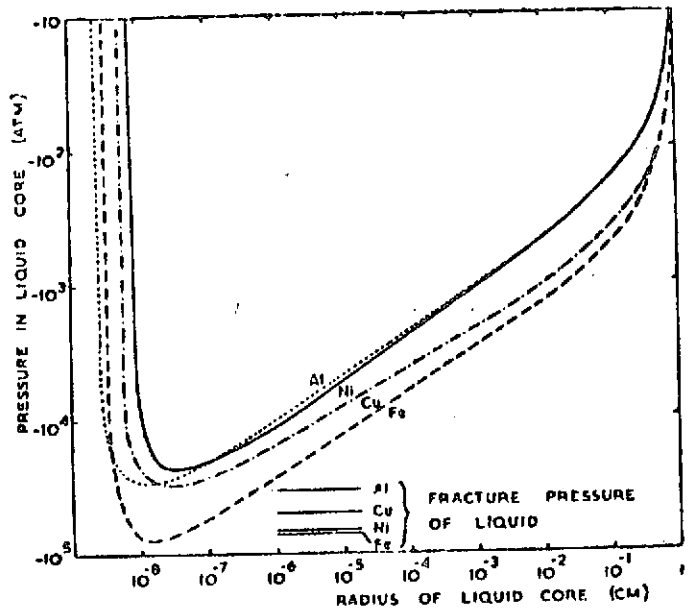

FIGURE 13. HYDROSTATIC TENSIONS IN THE LIQUID CORE OF 1 cm RADIUS CASTINGS OF ALUMINUM, COPPER, NICKEL, AND IRON CALCULATED FROM THE CREEP MODEL [36]

spheres in the M553 experiment are 0.32 cm in radius. The tensile pressures will be lesser in wide freezing range alloys [37].

Thus the value of possible shrinkage pressure developed within spherical solidifying castings has been evaluated for various materials exhibiting various deformation characteristics. The maximum attainable stresses in aluminum, copper, nickel and iron are in the range -10^4 to -10^{-5} atm. The exact values are uncertain because the solidification rate of a sphere is not accurately known, but it is probable that homogeneous nucleation is not a feasible mechanism for the initiation of porosity in solidifying metals. These extremely low pressures may help explain the unexpected results being found by other M553 contractor investigators.

G. FLIGHT RESULTS

A compilation of fluid velocities (on the molten sphere surfaces) measured from movies taken during Skylab, KC-135 aircraft and terrestrial processing is shown in Table 17. These velocities are measured by tracking oxide or shiny contaminant patches as they moved over the molten surfaces both before and after complete melting. Several KC-135 measurements were obtained even after release from the ceramic pedastals. Shown in the table are the surface velocity, processing environment, gravity level, date of processing, filming information, specimen identification and time of measurement relative to the melting sequence. Beam power data for all measurements were approximately 50 mA and 20 kV. The velocity measurements are accurate to within 20%. The variations in results are probably due to differences in material compositions and beam settings (i.e., focus, impact point, voltage and amperage) rather than gravity effects.

As shown earlier only surface tension and gravity forces are predicted to produce these velocities. The one velocity measurement obtainable from the Skylab movie was an order of magnitude lower than that obtained from some low gravity KC-135 aircraft and ground-based movies, but was similar to ground and KC-135 measurements also obtained long after complete melting. Thus it can be concluded that no significant difference in magnitude of convection occurred between Skylab, KC-135 and ground processing, which reinforces the theory of surface tension as the dominating force for fluid motion.

In addition to direct movie evidence of vigorous melt stirring, several other effects of convection were evident in metallurgical evaluations of Skylab specimens conducted by other investigators. The grain multiplication near the large shrinkage pore in the cap region of Skylab sample SL-1.6 (nickel-tin material) indicates vigorous flow probably due to solidification shrinkage[38]. Alumina was spread over the surface of SL-2.7[39] a release-type nickel-tin specimen, which supports the existence of vigorous convective stirring to transport the alumina from the pedestal. Similar findings of alumina transport were found on SL-1.8[40], a nickel-copper specimen.

Several Skylab samples possessed a large spherical or oblong cavity. These large interior cavities were usually associated with a "cap region" opposite the flat, epitaxial side of the specimens. These large pores are no doubt produced by the large shrinkage forces predicted to exist during Skylab processing.

Table 17

M553 SURFACE VELOCITY MEASUREMENTS

Processing Environment	Gravity Level* (g)	Date	Film (fps)**	Sphere Material	Fluid Velocity (m/sec)	Time of Measurement
Skylab	10^{-4}	6/15/73	Color, 24	Ni-Ag	0.02	Very long after melted
Ground	1	4/30/73	B&W, 3000	Ni-Ag	0.35 to 0.40	From early to complete melt
KC-135	$6 \cdot 10^{-3}$	7/25/72	Color, 200	Ni-Ag	0.20 0.10 0.06	Before full melt Right after full melt Long after full melt
Ground	1	10/20/72	B&W, 1000	Ni	0.15 0.20 0.33	Before complete melt
Ground	1	1972	Color, 200	Ni	0.12	Half melted

*1g = 9.8 m/sec^2

**fps = frames per second

H. CONCLUSIONS

The primary conclusion of the preceding discussions is that significant flow and stirring in the molten spheres (during and after eb melting) occurred in both terrestrial and space processing as predicted. The magnitude of this convective fluid motion was the same in both environments. The flow patterns, however, could not be quantitatively compared because the filming rate was too slow. Also, altered microstructure, increased grain refinement and the appearance of a single, large interior shrinkage pore have been found in the Skylab specimens as predicted. These effects can be traced to a longer duration containerless freezing than in ground and KC-135 flights; i.e., the surfaces opposite the expitaxial nucleation site were cooler than in the non-Skylab specimens (assuming release). These surfaces nucleated much sooner than their non-Skylab counterparts, thereby entrapping a larger enclosed pool of residual liquid. The solidification shrinkage forces, which cause fluid flow and tensile stresses (increased shrinkage porosity), were therefore much greater in the Skylab specimens even though all of the samples appeared to have some degree of unplanned, heterogeneous nucleation (retainment of unmelted material or solidified prior to release).

It should be noted that a repeat of this experiment in the microgravity environment of space as is, except for longer, higher speed camera coverage, would yield much more hydrodynamic information. This information is important because hydrodynamics controls the release of the specimens and affects the solidification and microstructure properties. The release mechanism is of utmost importance because it will control the duration of free float time in the absence of acoustic or electromagnetic levitation. It is also recommended that a new experiment be performed with no active mechanical forces (springs) for release, i.e., allow only the vaporization and electromagnetic forces to initiate release. The slight forces could be counteracted by the small residual gravity field to yield very slow release acceleration and extremely long free-float times.

REFERENCES

1. Laudise, R. A., Carruthers, J. R., and Jackson, K. A.: Crystal Growth, in Annual Review of Materials Science, Vol. 1, 1971, pp. 253-256.

2. Laudise, R. A.: The Growth of Single Crystals, Prentice-Hall, Englewood Cliffs, N. J., 1970, pp. 86-103.

3. Goldak, J. A., Burbidge, G., and Bibby, M. J.: Predicting Microstructure from Heat Flow Calculations in Electron Beam Welded Eutectoid Steels, Can. Met. Quart., Vol. 9, 1970, p. 459.

4. Ibid, p. 467.

5. Churchill, S. W., and Hellums, J. D., Dimensional Analysis and Natural Convection, Chem. Engr. Prog. Symp. Ser., Vol. 57, 1964, p. 75.

6. Ostrach, S.: Role of Analysis in the Solution of Complex Problems, Third Intl. Heat Trans. Conf., Chicago, August 1966.

7. Woods, R. A., and Milner, D. R.: Motion in the Weld Pool in Arc Welding, Welding J., April 1971, p. 163s.

8. Kotecki, D. J., Cheever, D. L., and Howden, D. G.: Mechanism of Ripple Formation During Weld Solidification, Welding J., August 1972, p. 386s.

9. Brimacombe, J. K., and Weinberg, F.: Surface Movements of Liquid Copper and Tin, Met. Trans., Vol. 3, 1972, p. 2298.

10. Torza, S., Cox, R. G., and Mason, S. G.: Electrohydrodynamic Deformation and Burst of Liquid Drops, Phil. Trans. Roy. Soc. London, Ser. A, Vol. 269, 1971, p. 295.

11. Berghmans, J.: Theoretical Investigation of the Interfacial Stability of Inviscid Fluids in Motion, Considering Surface Tension, J. Fluid Mech., Vol. 54, 1972, pp. 129-141.

12. Weber, C. M., Funk, E. R., and McMaster, R. C.: Penetration Mechanism of Partial Penetration Electron Beam Welding, Welding J., February 1972, pp. 90s-94s.

13. Tong, H., and Geidt, W. H.: A Dynamic Interpretation of Electron Beam Welding, Welding J., June 1970, pp. 259s-266s.

14. Bourgeois, S. V., and Brashears, M. R.: Fluid Dynamics and Kinematics of Molten Metals in the Low Gravity Environment of Skylab, AIAA Paper No. 74-205, Washington, D. C., 1 February 1974.

15. Tobin, J. M., and Kossowsky, R.: Final Report on M551, M552 and M553, Westinghouse Astronuclear Laboratory, Pittsburgh, Pa., WANL-L-854, Rev., 12 December 1973.

16. Paton, B. E.: Welding in Space, Welding Engineer, January 1972, pp. 25-29.

17. Bourgeois, S. V.: Convection in Skylab M512 Experiments M551, M552 and M553: Phase C Report, LMSC-HREC TR D306955, Lockheed Missiles & Space Company, Huntsville, Ala., December 1973.

18. Levich, V. G.: Physicochemical Hydrodynamics, Prentice-Hall, Englewood Cliffs, N. J., 1962.

19. Bird, R. B., Stewart, W. E., and Lightfoot, E. N.: Transport Phenomena, Wiley, New York, 1960, p. 54.

20. Prengle, R. S., and Rothfus, R. R.: Ind. Eng. Chem., Vol. 47, 1955, p. 379.

21. Young, N. O., Goldstein, J. S., and Block, M. J.: The Motion of Bubbles in a Vertical Temperature Gradient, J. Fluid Mech., Vol. 6, 1959, p. 356.

22. Blake, T. D., and Haynes, J. M.: Contact Angle Hysteresis, Progress in Surface and Membrane Science, Vol. 6, p. 131, 1973.

23. Rose, W., and Heins, R. W.: Moving Interfaces and Contact Angle Rate Dependency, J. Colloid Sci., Vol. 17, 1962, pp. 39-48.

24. Bikerman, J. J.: Surface Chemistry, Academic Press, New York, 1958, p. 360.

25. Petrash, D. A., and Otto, E. W.: Controlling the Liquid-Vapor Interface Under Weightlessness, Astronautics and Aeronautics, Vol. 2, No. 3, March 1964, pp. 56-61.

26. Schwartz, A. M.: Capillarity, Ind. Eng. Chem., Vol. 61, No. 1, 1969, pp. 10-21.

27. Braski, D. N., Adair, H. L. and Kobisk, E. H.: Radioisotope Tracer Studies in the NASA Skylab Exothermic Brazing Experiment M552, Oak Ridge National Laboratory, Oak Ridge, Tenn., December 1973.

28. Heine, R. W., Adams, C. M. and Siewert, T. A.: Report on Flight/Ground Sample Comparison Relating to Flight Experiment M552, Exothermic Brazing, University of Wisconsin, Madison, Wisc., 4 December 1973.

29. Lockheed Missiles & Space Company, Convection in Space Processing – Bimonthly Progress Report, LMSC-HREC D306219, 28 September 1972, p. B-9.

30. Lockheed Missiles & Space Company, Research Study on Materials Processing in Space Experiment M512 – Monthly Progress Report, LMSC-HREC PR D306549, Huntsville, Ala., 28 March 1973.

31. Brashears, M. R. and Robertson, S. J.: Research Study on Materials Processing in Space Experiment M512, Final Report, LMSC-HREC TR D306954, Lockheed Missiles & Space Company, Huntsville, Ala., 1 December 1973.

32. Parker, J. W., and Gatewood, E.: Sphere Float Time and Path for Skylab M553 Sphere Floating Experiment, NASA TM X (Preliminary).

33. Brashears, M. R.: Materials Processing in Space (M512), Monthly Progress Report, LMSC-HREC PR D306360, Lockheed Missiles & Space Company, Huntsville, Ala., December 1972.

34. Brashears, M. R.: Science and Engineering Information for M551 and M553 Experiments, LMSC-HREC TN D306615, Lockheed Missiles & Space Company, Inc., Huntsville, Ala., April 1973.

35. Campbell, J.: Shrinkage Pressure in Castings (The Solidification of a Metal Sphere), Trans. Met. Soc., AIME, Vol. 239, 1967, p. 138.

36. Campbell, J.: Hydrostatic Tensions in Solidifying Materials, Trans. Met. Soc., AIME, Vol. 242, 1968, p. 264.

37. Campbell, J.: Hydrostatic Tensions in Solidifying Alloys, Trans. Met. Soc., AIME, Vol. 242, 1968, p. 268.

38. Kattamis, T. Z.: Investigation of Solidification in Zero Gravity Environment; M553 Sphere Forming Experiment: Phase C Report, University of Connecticut, Storrs, Conn., 4 December 1973, p. 6.

39. Johnson, P. C., and Peters, E. T.: M553 Sphere Forming Experiment 90 Day Report, Contract NAS8-28723, A. D. Little, Inc., Cambridge, Mass., October 1973.

40. Hubbard, J. L., Johnson, J. W., and Brown, J. L.: Summary Report Phase C: Characterization of Four Specimens Processed as a Part of the M553 Sphere Forming Experiment, Georgia Institute of Technology, Atlanta, Ga., December 1973, p. 8.

ACKNOWLEDGEMENTS

The following reports were utilized extensively in compiling this summary document.

"Fluid Dynamics and Kinematics of Molten Metals in the Low-Gravity Environment of Skylab," S. V. Bourgeois and M. R. Brashears, paper presented at AIAA 12th Aerospace Sciences Meeting, Washington, D. C., 1 February 1974.

"Research Study on Materials Processing in Space Experiment M512: Final Report," LMSC-HREC TR D306954, M. R. Brashears and S. J. Robertson, Lockheed Missiles & Space Company, Huntsville, Ala., 1 December 1973.

"Convection Effects on Skylab Experiments M551, M552 and M553: Phase C Report," LMSC-HREC TR D306955, S. V. Bourgeois, Lockheed Missiles & Space Company, Huntsville, Ala., 1 December 1973.

"Report on Flight/Ground Sample Comparison Relating to Flight Experiment M552, Exothermic Brazing," R. W. Heine, C. M. Adams and T. A. Siewert, University of Wisconsin, Madison, 4 December 1973.

"Radioisotope Tracer Studies in the NASA Skylab Exothermic Brazing Experiment M552," D. N. Braski, H. L. Adair and E. H. Kobisk, Oak Ridge National Laboratory, Oak Ridge, Tenn., December 1973.

"Research Study on Materials Processing in Space Experiment Number M512: Final Report on M551, M552 and M553," WANL-L-854 Rev., J. M. Tobin and R. Kossowsky, Westinghouse Astronuclear Laboratory, Pittsburgh, Pa., 12 December 1973.

☆ U.S. GOVERNMENT PRINTING OFFICE 1974 – 640-446 / 109 REGION NO. 4